Spatiotemporal Subpixel Mapping Based on Priori Remote Sensing Image With Variation Differences

Peng Wang ⓘ, *Member, IEEE*, Mingxuan Huang, Liguo Wang ⓘ, Gong Zhang ⓘ, *Member, IEEE*, Henry Leung ⓘ, *Fellow, IEEE*, and Chunlei Zhao ⓘ

Abstract—Subpixel mapping (SPM) could handle the mixed pixels in coarse original spectral image (COSI) to obtain the fine land-cover class mapping result. In recent years, with the auxiliary spatiotemporal information provided by the same region fine prior spectral image (FPSI), spatiotemporal subpixel mapping (SSPM) has shown greater potential than the traditional SPM methods. However, the inaccurate spatiotemporal information of the FPSI is rarely effective identified due to variation differences in the current SSPM methods, affecting the mapping accuracy. To address the abovementioned issues, SSPM based on priori remote sensing image with variation differences (CVDBI) is proposed. First, the coarse abundance images of COSI and the fine thematic images of FPSI are obtained by unmixing COSI and classifying FPSI. Second, the degradation observation model (DOM) is established to use downsampling matrix to correlate the coarse abundance images of COSI with the ideal thematic images of COSI, and the variation difference observation model (VDOM) is established to use variation difference factor to correlate the fine thematic images of FPSI with the ideal thematic images of COSI. Third, a separable convex optimization model is established for DOM and VDOM. This model optimizes the variation difference factor and the ideal thematic images of COSI. Finally, we use the alternating direction method of multipliers to solve the separable convex optimization problem to produce the final mapping result. Experimental results on the three spectral images show that the proposed CVDBI yields the more accurate mapping result than the traditional SPM methods.

Index Terms—Alternating direction method of multipliers, separable convex optimization model, spatiotemporal subpixel mapping, spectral imagery, variation difference.

I. INTRODUCTION

IN THE context of remote sensing big data, multitemporal and multisource spectral images (multi- and hyperspectral images) are widely utilized in land-cover classes mapping due to its abundant spectral information [1], [2]. The land-cover classes mapping information is important for ecosystem protection and environmental monitoring [3]. However, due to the complexity of the distribution of land-cover classes and the limitations of remote sensing platform hardware, the spectral image sometimes contains lots of mixed pixels, which are the main factors restricting the spatial resolution of spectral image [4]. Although classification technique could handle the spectral image at pixel level to obtain the land-cover classes mapping information [5] by assigning one land-cover class label to one pixel, one mixed pixel often contains more than one land-cover class, resulting in challenge for the classification technique [6], [7], [8].

The flowchart of mixed pixels processing is shown in Fig. 1. Although the coarse original spectral image (COSI) acquired at T2 can be handled to produce the coarse abundance images with the proportion information of mixed pixels belonging to land-cover classes by spectral unmixing technology, the specific spatial distribution information of land-cover classes is still uncertain [9], [10]. To address this issue, subpixel mapping (SPM) technology is proposed as the follow-up processing step of spectral unmixing. According to a scale factor S, SPM first transforms the coarse abundance image for each class to the ideal thematic image for each class by segmenting each mixed pixel into $S \times S$ subpixels. The final mapping result with the specific spatial distribution information of land-cover classes is obtained by assigning the corresponding class label to the ideal thematic
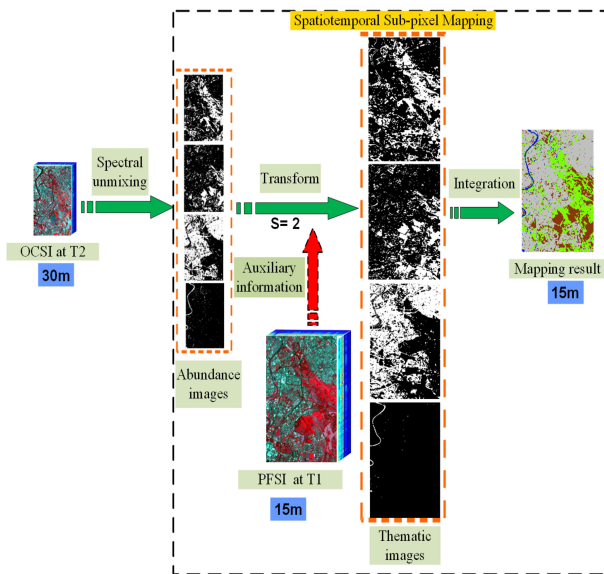
Fig. 1. Flowchart of mixed pixels processing.

images and then integrating these ideal thematic images [11]. It is worth noting that in recent years, under the background of remote sensing big data, spatiotemporal subpixel mapping (SSPM) utilizes the auxiliary spatiotemporal information from the fine prior spectral image (FPSI) in the same region acquired at T1 to produce better mapping result and shows greater potential than the traditional SPM methods [12].

In the past two decades, SPM has been widely applied to many fields, such as building extraction [13], flood inundation mapping [14], burned-area mapping [15], forest cover monitor [16], and change detection [17]. Atkinson [18] first proposed the concept of SPM, and since then SPM has been developed into a variety of practical methods. The traditional SPM methods are usually based on monotemporal image and could be divided into two main types according to the way of obtaining the mapping result [19]. One type is the initialization-then-optimization SPM (ITO-SPM). ITO-SPM randomly assigns land-cover classes labels to subpixels, and then optimizes the location of each subpixel to obtain the final mapping result. SPM methods based on pixel swapping model [20], perimeter minimization [21], genetic algorithm [22], and particle swarm optimization [23] all belong to this type. The other type is the soft-then-hard SPM (STHSPM). STHSPM improves the coarse abundance images to produce the ideal abundance images with the land-cover classes proportions corresponding to subpixels by subpixel sharpening, and then assigns the land-cover classes labels to subpixels according to these proportions, deriving the final mapping result. SPM methods based on backpropagation neural network [24], [25], spatial attraction model [26], [27], Hopfield neural networks [28], [29], interpolation algorithm [30], [31], indicator cokriging [32], [33], object dependence [34], [35], geographical objects [36], units of classes [37], and hybrid constraints of pure and mixed pixels [38] all belong to this type. In addition to the above two main SPM types, deep learning has been successfully

applied to SPM in recent years [39], [40], [41]. However, SPM based on deep learning usually needs a lot of fine training data to achieve the desired performance, in the absence of a large number of fine training data, the two main SPM types show better performance.

Because SPM is an ill posed inverse problem [42], the traditional SPM methods based on monotemporal image usually lack *a priori* knowledge of the actual geographical distribution to constrain the fuzziness and uncertainty of the results, which will affect the accuracy of SPM result. In order to solve this problem, the SSPM proposed in recent years uses the appropriate FPSI as the prior knowledge constraint, which is widely used to solve the ill posed inverse problem of SPM. Therefore, SSPM as a novel SPM model shows greater potential and application prospects. Ling et al. [43] proposed the concept of SSPM. SSPM is then further developed and applied to the traditional spatial attraction model, pixel swapping model, and Hopfield neural network [44], [45], [46]. In recent years, SSPM based on spatial-temporal dependence method is proposed, which usually utilizes spatial-temporal dependence to establish a spatiotemporal objective, and then optimizes the objective to obtain a reasonable spatial distribution of land-cover classes at subpixel scale [47], [12]. Subsequently, SSPM based on spatial-temporal dependence method is further extended to utilize spatial-temporal-spectral dependence to establish the spatiotemporal objective [48]. In addition, Wang et al. [49] and He et al. [50] utilized point spread function effect and MAP model to improve the performance of SSPM.

However, the conventional SSPM methods generally need the acquisition time of COSI and FPSI to be as close as possible to ensure that the spatial distribution of the two images is similar, so that the FPSI can provide accurate auxiliary spatiotemporal information. Due to the periodicity of remote sensing satellite operation and the variability of land-cover classes, there will be some variation differences in land-cover changes between COSI and FPSI. Especially, there is sometimes only FPSI with large variation difference provided. Therefore, the conventional SSPM methods are difficult to effectively identify the inaccurate spatiotemporal information of the FPSI due to variation differences, resulting in reducing the accuracy of land-cover classes mapping. To overcome the abovementioned problems, a SSPM based on priori remote sensing image with variation differences (CVDBI) is proposed. Since the fractional images are the results of spectral unmixing for spectral image, the variation differences between COSI and FPSI are defined by measuring the differences between their fractional images in this article. In CVDBI, the variation difference factor is proposed to construct a separable convex optimization model to effectively recognize the inaccurate spatiotemporal information of FPSI, so as to improve the accuracy of final mapping result. Experimental results show the superiority of the CVDBI over the state-of-the-art SPM methods.

The contributions of this article are as follows.
1) The inaccurate spatiotemporal information of FPSI is effectively recognized in CVDBI to improve the performance of SSPM and obtain the high accuracy mapping result.
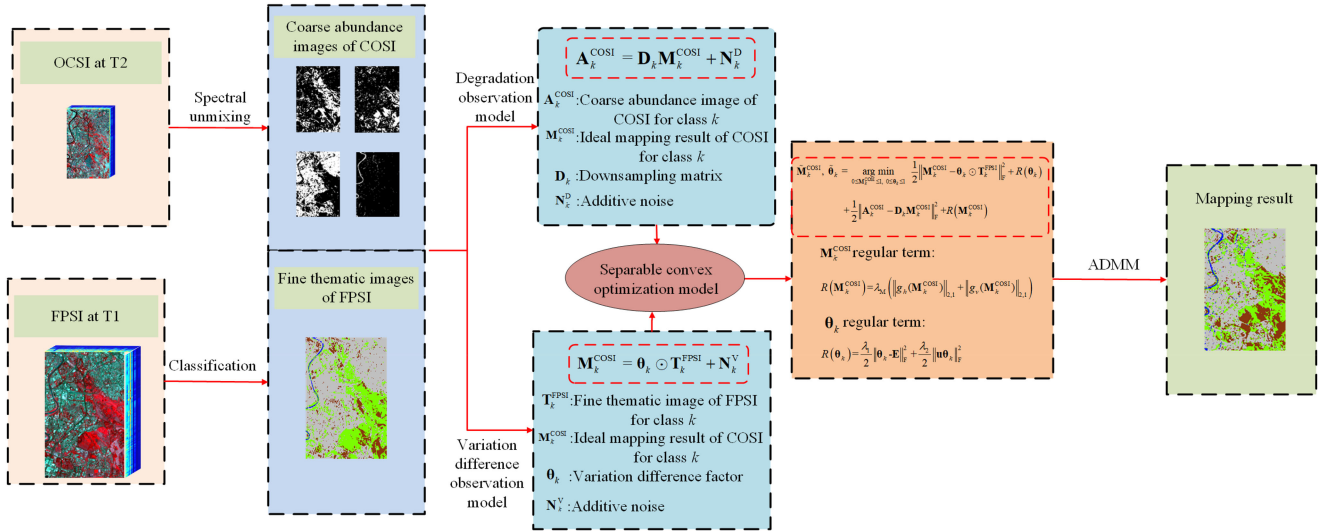
Fig. 2.   Flowchart of CVDBI.

2) CVDBI could show the ideal performance by using the FPSI captured at various times in order to relieve the limitations of the close acquisition time of COSI and FPSI in the current SSPM methods.

3) Even if there is a large variation difference between COSI and FPSI, CVDBI also could be used to obtain the ideal mapping result due to the variation difference factor. Therefore, CVDBI could be effectively applied to large variation difference scenes where the time interval of collecting between COSI and FPSI is long, or the frequency of disaster change between COSI and FPSI is high.

The rest of this article is organized as follows. The proposed method is described in Section II. The experimental results are presented qualitatively and quantitatively in Section III. Discussion is introduced in Section IV. Finally, Section V concludes this article.

II. METHODOLOGY

The flowchart of CVDBI is shown in Fig. 2. First, COSI at T2 is unmixed to produce the coarse abundance images of COSI, and FPSI at T1 is classified to obtain the classification result, which provides the fine thematic images of FPSI. Second, the coarse abundance image of COSI for each class is correlated with the ideal thematic image of COSI for each class by downsampling matrix in the degradation observation model (DOM), and the fine thematic image of FPSI for each class is correlated with the ideal thematic image of COSI for each class by variation difference factor in the variation difference observation model (VDOM). Third, CVDBI establishes a separable convex optimization model for DOM and VDOM to optimize the variation difference factor and the ideal thematic image of COSI. Finally, alternating direction method of multipliers (ADMM) is utilized to solve the separable convex optimization problem to derive the mapping result. This section will introduce the proposed method in detail.
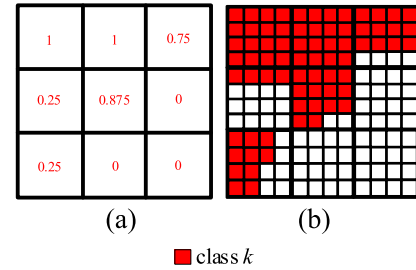
Fig. 3.   Example of DOM. (a) Coarse abundance image of COSI for class k. (b) Ideal thematic image of COSI for class k.

A. Observation Model Construction

Suppose $\mathbf{Z}^{\text{COSI}} \in \mathbf{R}^{B \times N}$ is COSI at T2, with B spectral bands and N pixels, $\mathbf{Z}^{\text{FPSI}} \in \mathbf{R}^{B \times NS^2}$ is FPSI at T1, with B spectral bands and NS^2 pixels, S is the scale factor of the two images. $\mathbf{Z}^{\text{COSI}}$ is unmixed to obtain the coarse abundance image of COSI $\mathbf{A}_k^{\text{COSI}} \in \mathbf{R}^{P \times N}$ ($k = 1, 2, \ldots, K$, K is the number of land-cover classes) for class k, P is the number of pure substances at the endmember. $\mathbf{Z}^{\text{FPSI}}$ is classified to provide the fine thematic image of FPSI $\mathbf{T}_k^{\text{FPSI}} \in \mathbf{R}^{P \times NS^2}$ for class k. $\mathbf{M}_k^{\text{COSI}} \in \mathbf{R}^{P \times NS^2}$ is the ideal thematic image of COSI for class k, and the SPM result can be considered as the result of the integration of the ideal thematic images of COSI for all land-cover classes [51].

In CVDBI, two different types of observation models (DOM and VDOM) are established. In the DOM, to consider the spatial degradation between the coarse abundance image of COSI and the ideal thematic image of COSI, the coarse abundance image of COSI $\mathbf{A}_k^{\text{COSI}}$ for class k and the ideal thematic image of COSI $\mathbf{M}_k^{\text{COSI}}$ for class k are linked by spatial downsampling matrix $\mathbf{D}_k \in \mathbf{R}^{NS^2 \times N}$ with the scale factor S [50]. The DOM is illustrated in Fig. 3 by a simple example. As shown in Fig. 3(a), the coarse abundance image of COSI $\mathbf{A}_k^{\text{COSI}}$ for class k includes nine mixed pixels marked with the proportions of class k (red number). Fig. 3(b) shows the ideal thematic image of COSI $\mathbf{M}_k^{\text{COSI}}$ for class k. Here, the downsampling scale S is 4, and the

downsampling matrix $\mathbf{D}_k$ is an averaging filter, where all the elements are equal to $1/S^2$, i.e., 1/16 in this case. For instance, 0.875 in the central pixel in Fig. 3(a) indicates that $16 \times 0.875 = 14$ subpixels within the central pixel belong to class k in Fig. 3(b). Therefore, in the DOM, we use the downsampling matrix $\mathbf{D}_k$ to correlate the coarse abundance image with the ideal thematic image as follows:

$$\mathbf{A}_k^{\text{COSI}} = \mathbf{D}_k \mathbf{M}_k^{\text{COSI}} + \mathbf{N}_k^{\text{D}} \tag{1}$$

where $\mathbf{N}_k^{\text{D}} \in \mathbf{R}^{P \times N}$ represents the additive noise in the DOM.

In the VDOM, to consider the variation differences between COSI and FPSI, the variation factor $\boldsymbol{\theta}_k$ is proposed to establish the relationship between the fine thematic image of FPSI $\mathbf{T}_k^{\text{FPSI}}$ for class k and the ideal thematic image of COSI $\mathbf{M}_k^{\text{COSI}}$ for class k. Therefore, the VDOM can be expressed as

$$\mathbf{M}_k^{\text{COSI}} = \boldsymbol{\theta}_k \odot \mathbf{T}_k^{\text{FPSI}} + \mathbf{N}_k^{\text{V}} \tag{2}$$

where $\odot$ is the multiplication of the elements, $\mathbf{N}_k^{\text{V}} \in \mathbf{R}^{P \times NS^2}$ is the additive noise in the VDOM. $\mathbf{N}_k^{\text{V}}$ and $\mathbf{N}_k^{\text{D}}$ are all constructed as Gaussian white noise, but with different sizes.

B. Separable Convex Optimization Model

A separable convex optimization model is established for (1) and (2) to realize SSPM, as shown in

$$\tilde{\mathbf{M}}_k^{\text{COSI}}, \tilde{\theta}_k$$
$$= \underset{0 \leq \mathbf{M}_k^{\text{COSI}} \leq 1, 0 \leq \boldsymbol{\theta}_k \leq 1}{\arg\min} \frac{1}{2} \left\| \mathbf{M}_k^{\text{COSI}} - \boldsymbol{\theta}_k \odot \mathbf{T}_k^{\text{FPSI}} \right\|_{\text{F}}^2 + R(\boldsymbol{\theta}_k)$$
$$+ \frac{1}{2} \left\| \mathbf{A}_k^{\text{COSI}} - \mathbf{D}_k \mathbf{M}_k^{\text{COSI}} \right\|_{\text{F}}^2 + R(\mathbf{M}_k^{\text{COSI}}) \tag{3}$$

where $R(\mathbf{M}_k^{\text{COSI}})$ is the regularization term of the ideal thematic image of COSI $\mathbf{M}_k^{\text{COSI}}$ for class k, $R(\boldsymbol{\theta}_k)$ is the regularization term of the variation factor $\boldsymbol{\theta}_k$.

The regularization term $R(\mathbf{M}_k^{\text{COSI}})$ is based on gradient $L_{2,1}$ norm to improve sparsity of the gradient across different materials, as shown in

$$R(\mathbf{M}_k^{\text{COSI}}) = \lambda_{\text{M}} \left(\left\| g_h(\mathbf{M}_k^{\text{COSI}}) \right\|_{2,1} + \left\| g_v(\mathbf{M}_k^{\text{COSI}}) \right\|_{2,1} \right) \tag{4}$$

where the linear operators $g_h(\textbf{.})$ and $g_v(\textbf{.})$ calculate the ideal thematic image of COSI $\mathbf{M}_k^{\text{COSI}}$ for class k in the first-order horizontal and vertical gradients, respectively. λ_{M} balances the contribution of the regularization term $R(\mathbf{M}_k^{\text{COSI}})$ to (3).

The regularization term $R(\boldsymbol{\theta}_k)$ is realized by gradient L_2 norm and defined as

$$R(\boldsymbol{\theta}_k) = \frac{\lambda_1}{2} \left\| \boldsymbol{\theta}_k - \mathbf{E} \right\|_{\text{F}}^2 + \frac{\lambda_2}{2} \left\| \mathbf{u} \boldsymbol{\theta}_k \right\|_{\text{F}}^2, \tag{5}$$

where the first term controls the variation factor $\boldsymbol{\theta}_k$ by limiting it to close to 1, $\mathbf{E}$ is a matrix with all elements of 1. The second term enhances the smoothness of the variation factor $\boldsymbol{\theta}_k$ by the differential operator $\mathbf{u}$. λ_1 and λ_2 balance the contribution of the regularization term $R(\boldsymbol{\theta}_k)$ to (3).

C. Obtaining Mapping Result

Separable convex optimization model in (3) is individually convex for each variable (the ideal thematic image of COSI $\mathbf{M}_k^{\text{COSI}}$ and the variation factor $\boldsymbol{\theta}_k$). Therefore, we use the ADMM to solve the separable convex optimization problem [51], [52]. ADMM implements the distributed optimization strategy to iteratively minimize the cost function of each variable to find the local stationary point.

In order to use ADMM, the cost function in (3) need be defined in the following form:

$$\min_{\mathbf{x}, \mathbf{y}} \left\{ f(\mathbf{x}) + g(\mathbf{y}) \,|\, \mathbf{A}\mathbf{x} + \mathbf{B}\mathbf{y} = \mathbf{C} \right\} \tag{6}$$

where $f : \mathbb{R}^a \to \mathbb{R}^+$ and $g : \mathbb{R}^b \to \mathbb{R}^+$ are closed-convex functions. $\mathbf{x} \in \mathbb{R}^a$ and $\mathbf{y} \in \mathbb{R}^b$ are nonempty closed convex sets including vector variables. $\mathbf{A} \in \mathbb{R}^{c \times a}, \mathbf{B} \in \mathbb{R}^{c \times b}$, and $\mathbf{C} \in \mathbb{R}^c$ have full column ranks.

The augmented Lagrange function is defined to use the scaled formulation of ADMM and is given by

$$L(\mathbf{x}, \mathbf{y}, \mathbf{z}) = f(\mathbf{x}) + g(\mathbf{y}) + \frac{\beta}{2} \left\| \mathbf{A}\mathbf{x} + \mathbf{B}\mathbf{y} - \mathbf{C} + \mathbf{z} \right\|_{\text{F}}^2 \tag{7}$$

where $\mathbf{z} \in \mathbb{R}^c$ is the Lagrange multipliers in a vector form and β is a penalty parameter.

The ADMM updates the variables $\mathbf{x}, \mathbf{y}$, and $\mathbf{z}$ through multiple iterations. Suppose that $\mathbf{x}^{(i)}, \mathbf{y}^{(i)}$, and $\mathbf{z}^{(i)}$ are the variables at the ith iteration of the algorithm, the iterative scheme of ADMM is defined as the following procedure:

$$\mathbf{x}^{(i+1)} = \underset{\mathbf{x}}{\arg\min} \, L\left(\mathbf{x}, \mathbf{y}^{(i)}, \mathbf{z}^{(i)} \right)$$
$$\mathbf{y}^{(i+1)} = \underset{\mathbf{y}}{\arg\min} \, L\left(\mathbf{x}^{(i)}, \mathbf{y}, \mathbf{z}^{(i)} \right)$$
$$\mathbf{z}^{(i+1)} = \mathbf{z}^{(i)} + \mathbf{A}\mathbf{x}^{(i+1)} + \mathbf{B}\mathbf{y}^{(i+1)} - \mathbf{C}. \tag{8}$$

It can be found that the variables $\mathbf{x}$ and $\mathbf{y}$ are updated alternately. It is worth noting that when ADMM optimizes the $\mathbf{M}_k^{\text{COSI}}$ or $\boldsymbol{\theta}_k$, another variable is known and fixed, so each iteration is equivalent to solving only one variable. Here, we initialize $\boldsymbol{\theta}_k^{(0)} = \mathbf{E}$ and $\mathbf{M}_k^{\text{COSI}(0)}$ with SPM based on spatial attraction model for $\mathbf{A}_k^{\text{COSI}}$. This solution is presented in Algorithm 1. Next, we introduce the optimization process for variables $\boldsymbol{\theta}_k$ and $\mathbf{M}_k^{\text{COSI}}$.

1) Optimizing $\boldsymbol{\theta}_k$: Considering $\mathbf{M}_k^{\text{COSI}}$ fixed, the optimization process of $\boldsymbol{\theta}_k$ can be recast from (3) by considering only terms that depend on $\boldsymbol{\theta}_k$

$$\tilde{\boldsymbol{\theta}}_k = \underset{0 \leq \boldsymbol{\theta}_k \leq 1}{\arg\min} \frac{1}{2} \left\| \mathbf{M}_k^{\text{COSI}} - \boldsymbol{\theta}_k \odot \mathbf{T}_k^{\text{FPSI}} \right\|_{\text{F}}^2 + i_+(\boldsymbol{\theta}_k)$$
$$+ \frac{\lambda_1}{2} \left\| \boldsymbol{\theta}_k - \mathbf{E} \right\|_{\text{F}}^2 + \frac{\lambda_2}{2} \left\| \mathbf{u} \boldsymbol{\theta}_k \right\|_{\text{F}}^2 \tag{9}$$

where $i_+(\textbf{.})$ is the indicator function of the nonnegative $\mathbb{R}^+$ implementing a positive constraint, and is defined as $i_+(a) = \begin{cases} 0, a \geq 0 \\ \infty, a < 0 \end{cases}$.

In order to be equivalent to the ADMM problem, the (9) is re-expressed as

$$\tilde{\boldsymbol{\theta}}_k = \underset{0 \leq \boldsymbol{\theta}_k \leq 1}{\operatorname{argmin}} \frac{1}{2} \left\| \mathbf{M}_k^{\mathrm{COSI}} - \mathbf{G} \right\|_{\mathrm{F}}^2 + i_+ \left(\boldsymbol{\theta}_k \right)$$

$$+ \frac{\lambda_1}{2} \left\| \boldsymbol{\theta}_k - \mathbf{E} \right\|_{\mathrm{F}}^2 + \frac{\lambda_2}{2} \left\| \mathbf{u} \boldsymbol{\theta}_k \right\|_{\mathrm{F}}^2 \quad (10)$$

where $\mathbf{G} = \boldsymbol{\theta}_k \odot \mathbf{T}_k^{\mathrm{FPSI}}$.

To use the augmented Lagrange function $L(\mathbf{x}, \mathbf{y}, \mathbf{z})$, we define the following relationship:

$$\mathbf{x} = \mathrm{vec}\left(\boldsymbol{\theta}_k\right) \quad \mathbf{y} = \mathrm{vec}\left(\mathbf{G}\right)$$

$$\mathbf{A} = -\mathrm{dia}\left(\mathrm{vec}\left(\mathbf{T}_k^{\mathrm{FPSI}}\right) \right) \quad \mathbf{B} = \mathbf{I} \quad (11)$$

where $\mathrm{vec}(\boldsymbol{.})$ is the vectorization version by concatenating its columns, $\mathrm{dia}(\boldsymbol{.})$ is diagonal matrix with $\mathrm{vec}(\mathbf{T}_k^{\mathrm{FPSI}})$ in the main diagonal, and $\mathbf{I}$ is the identity matrix.

The augmented Lagrange function for (10) is written as

$$L\left(\boldsymbol{\theta}_k, \mathbf{G}, \mathbf{z}\right) = \frac{1}{2} \left\| \mathbf{M}_k^{\mathrm{COSI}} - \mathbf{G} \right\|_{\mathrm{F}}^2 + \frac{\lambda_1}{2} \left\| \boldsymbol{\theta}_k - \mathbf{E} \right\|_{\mathrm{F}}^2 + \frac{\lambda_2}{2} \left\| \mathbf{u} \boldsymbol{\theta}_k \right\|_{\mathrm{F}}^2$$

$$+ \frac{\beta}{2} \left\| -\boldsymbol{\theta}_k \odot \mathbf{T}_k^{\mathrm{FPSI}} + \mathbf{G} + \mathbf{z} \right\|_{\mathrm{F}}^2 + i_+ \left(\boldsymbol{\theta}_k \right). \quad (12)$$

When utilizing $L(\boldsymbol{\theta}_k, \mathbf{G}, \mathbf{z})$ to optimize the variable $\boldsymbol{\theta}_k$, the indicator function $i_+(\boldsymbol{\theta}_k)$ is ignored for simplicity and (12) can be re-expressed as

$$\tilde{\boldsymbol{\theta}}_k = \underset{0 \leq \boldsymbol{\theta}_k \leq 1}{\operatorname{argmin}} \frac{\lambda_1}{2} \left\| \boldsymbol{\theta}_k - \mathbf{E} \right\|_{\mathrm{F}}^2 + \frac{\lambda_2}{2} \left\| \mathbf{u} \boldsymbol{\theta}_k \right\|_{\mathrm{F}}^2$$

$$+ \frac{\beta}{2} \left\| -\boldsymbol{\theta}_k \odot \mathbf{T}_k^{\mathrm{FPSI}} + \mathbf{G} + \mathbf{z} \right\|_{\mathrm{F}}^2. \quad (13)$$

We take the derivative $\boldsymbol{\theta}_k$ in (13) and set it equal to 0 to derive

$$\left(\lambda_1 + \lambda_2 \mathbf{u}^{\mathrm{T}} \mathbf{u} + \beta \left(\mathbf{T}_k^{\mathrm{FPSI}} \odot \mathbf{T}_k^{\mathrm{FPSI}} \right) \right) \boldsymbol{\theta}_k$$

$$= \lambda_1 \mathbf{E} + \beta \left(\mathbf{T}_k^{\mathrm{FPSI}} \odot \mathbf{G} + \mathbf{T}_k^{\mathrm{FPSI}} \odot \mathbf{z} \right). \quad (14)$$

Equation (14) is solved efficiently due to the sparsity in the matrices on the left-hand side. The solution $\boldsymbol{\theta}_k$ by solving (14) is introduced into (15) to obtain the ideal variation factor $\tilde{\boldsymbol{\theta}}_k$

$$\tilde{\boldsymbol{\theta}}_k = \max\left(\boldsymbol{\theta}_k, 0\right). \quad (15)$$

The optimization of $L(\boldsymbol{\theta}_k, \mathbf{G}, \mathbf{z})$ with respect to other variables $\mathbf{G}$ and $\mathbf{z}$ is described in Appendix A.

2) Optimizing $\mathbf{M}_k^{\mathrm{COSI}}$: According to (3), the optimization process of $\mathbf{M}_k^{\mathrm{COSI}}$ can be defined as (16) for a fixed $\boldsymbol{\theta}_k$

$$\tilde{\mathbf{M}}_k^{\mathrm{COSI}} = \underset{0 \leq \mathbf{M}_k^{\mathrm{COSI}} \leq 1}{\operatorname{argmin}} \frac{1}{2} \left\| \mathbf{M}_k^{\mathrm{COSI}} - \boldsymbol{\theta}_k \odot \mathbf{T}_k^{\mathrm{FPSI}} \right\|_{\mathrm{F}}^2$$

$$+ \frac{1}{2} \left\| \mathbf{A}_k^{\mathrm{COSI}} - \mathbf{D}_k \mathbf{M}_k^{\mathrm{COSI}} \right\|_{\mathrm{F}}^2$$

$$+ \lambda_{\mathrm{M}} \left(\left\| g_h(\mathbf{M}_k^{\mathrm{COSI}}) \right\|_{2,1} + \left\| g_v(\mathbf{M}_k^{\mathrm{COSI}}) \right\|_{2,1} \right)$$

$$+ i_+ \left(\mathbf{M}_k^{\mathrm{COSI}} \right). \quad (16)$$

Algorithm 1

Input: $\mathbf{A}_k^{\mathrm{COSI}}$, $\mathbf{T}_k^{\mathrm{FPSI}}$ parameters λ_{M}, λ_1 and λ_2.

Output: The ideal variation factor $\tilde{\boldsymbol{\theta}}_k$ and the ideal thematic image of COSI $\tilde{\mathbf{M}}_k^{\mathrm{COSI}}$.

Initialize $\boldsymbol{\theta}_k^{(0)} = \mathbf{E}$;

Initialize $\mathbf{M}_k^{\mathrm{COSI}(0)}$ with SPM based on spatial attraction model for $\mathbf{A}_k^{\mathrm{COSI}}$;

Set $i = 0$;

While stopping criterion is not satisfied **do:**

  $i = i + 1$;

  Compute $\boldsymbol{\theta}_k^{(i)}$ by solving (9) using $\mathbf{M}_k^{\mathrm{COSI}(i)} \equiv \mathbf{M}_k^{\mathrm{COSI}(i-1)}$;

  Compute $\mathbf{M}_k^{\mathrm{COSI}(i)}$ by solving (16) using $\boldsymbol{\theta}_k^{(i)} \equiv \boldsymbol{\theta}_k^{(i-1)}$;

end

return $\tilde{\boldsymbol{\theta}}_k$, $\tilde{\mathbf{M}}_k^{\mathrm{COSI}}$;

The following variables are defined to represent optimization problem (16) in the form of (6):

$$\mathbf{G}_1 = \mathbf{D}_k \mathbf{G}_2 \quad \mathbf{G}_2 = \mathbf{M}_k^{\mathrm{COSI}}$$

$$\mathbf{G}_3 = g_h(\mathbf{G}_2) \quad \mathbf{G}_4 = g_v(\mathbf{G}_2)$$

$$\mathbf{G}_5 = \mathbf{M}_k^{\mathrm{COSI}}. \quad (17)$$

Equation (16) is then represented as

$$\tilde{\mathbf{M}}_k^{\mathrm{COSI}} = \underset{0 \leq \mathbf{M}_k^{\mathrm{COSI}} \leq 1}{\operatorname{argmin}} \frac{1}{2} \left\| \mathbf{M}_k^{\mathrm{COSI}} - \boldsymbol{\theta}_k \odot \mathbf{T}_k^{\mathrm{FPSI}} \right\|_{\mathrm{F}}^2 + i_+ \left(\mathbf{G}_5 \right)$$

$$+ \lambda_{\mathrm{M}} \left(\left\| \mathbf{G}_3 \right\|_{2,1} + \left\| \mathbf{G}_4 \right\|_{2,1} \right) + \frac{1}{2} \left\| \mathbf{A}_k^{\mathrm{COSI}} - \mathbf{G}_1 \right\|_{\mathrm{F}}^2. \quad (18)$$

The following relationship is defined to use augmented Lagrange function $L(\mathbf{x}, \mathbf{y}, \mathbf{z})$:

$$\mathbf{x} = \mathrm{vec}\left(\mathbf{M}_k^{\mathrm{COSI}}\right)$$

$$\mathbf{y} = \left[\mathrm{vec}\left(\mathbf{G}_1\right) \; \mathrm{vec}\left(\mathbf{G}_2\right) \; \mathrm{vec}\left(\mathbf{G}_3\right) \; \mathrm{vec}\left(\mathbf{G}_4\right) \; \mathrm{vec}\left(\mathbf{G}_5\right) \right]^{\mathrm{T}}$$

$$\mathbf{A} = \left[\mathrm{r}(\mathbf{D}_k) \; \mathbf{I} \; \mathbf{0} \; \mathbf{0} \; \mathbf{I} \right]^{\mathrm{T}}$$

$$\mathbf{B} = \begin{bmatrix} -\mathbf{I} & \mathbf{0} & \mathbf{0} & \mathbf{0} & \mathbf{0} \\ \mathbf{0} & -\mathbf{I} & \mathbf{0} & \mathbf{0} & \mathbf{0} \\ \mathbf{0} & \mathbf{G}_h & -\mathbf{I} & \mathbf{0} & \mathbf{0} \\ \mathbf{0} & \mathbf{G}_v & \mathbf{0} & -\mathbf{I} & \mathbf{0} \\ \mathbf{0} & \mathbf{0} & \mathbf{0} & \mathbf{0} & -\mathbf{I} \end{bmatrix} \quad (19)$$

where $\mathrm{r}(\mathbf{D}_k)$ is defined that $\mathrm{r}(\mathbf{D}_k)\mathrm{vec}(\mathbf{M}_k^{\mathrm{COSI}}) = \mathbf{D}_k \mathbf{M}_k^{\mathrm{COSI}}$. $\mathbf{G}_h$ and $\mathbf{G}_v$ are their matrices of the linear operators $g_h(\boldsymbol{.})$ and $g_v(\boldsymbol{.})$.

Therefore, the augmented Lagrange function is defined as

$$L\left(\mathbf{x}, \mathbf{y}, \mathbf{z}\right) = \frac{1}{2} \left\| \mathbf{x} - \mathrm{vec}\left(\boldsymbol{\theta}_k \odot \mathbf{T}_k^{\mathrm{FPSI}} \right) \right\|_{\mathrm{F}}^2$$

$$+ \frac{1}{2} \left\| \mathrm{vec}\left(\mathbf{A}_k^{\mathrm{COSI}}\right) - \mathrm{vec}\left(\mathbf{G}_1\right) \right\|_{\mathrm{F}}^2$$

$$+ \lambda_{\mathrm{M}} \left(\left\| \mathbf{G}_3 \right\|_{2,1} + \left\| \mathbf{G}_4 \right\|_{2,1} \right) + i_+ \left(\mathbf{G}_5 \right)$$
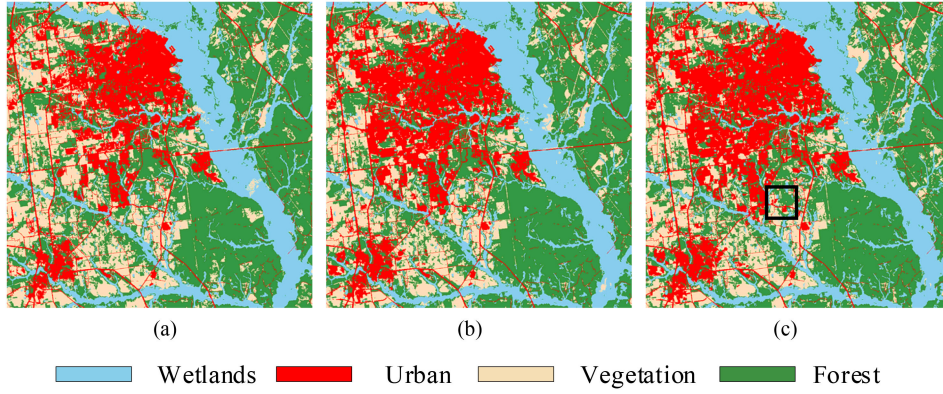
Fig. 4. Synthetic data set 1. (a) NLCD 2001. (b) NLCD 2006. (c) NLCD 2011.
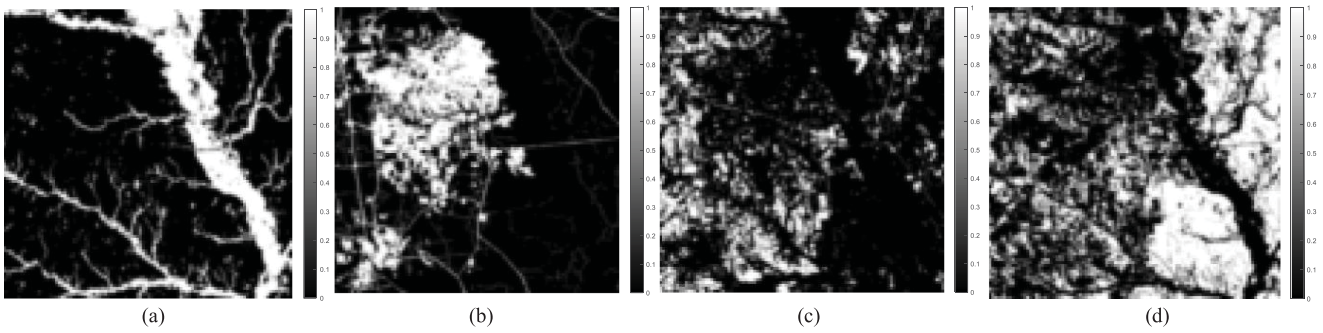

Fig. 5. Abundance images of NLCD 2011: from (a)–(d): Wetlands, Urban, Vegetation and Forest ($S = 8$).

$$+\frac{\beta}{2}\left\|\mathrm{r}(\mathbf{D}_k)\mathbf{x} - \mathrm{vec}\,(\mathbf{G}_1) + \mathbf{z}_1\right\|_{\mathrm{F}}^2$$

$$+\frac{\beta}{2}\left\|\mathbf{x} - \mathrm{vec}\,(\mathbf{G}_2) + \mathbf{z}_2\right\|_{\mathrm{F}}^2 + \frac{\beta}{2}\left\|\mathbf{G}_h\mathrm{vec}\,(\mathbf{G}_2) - \mathrm{vec}\,(\mathbf{G}_3) + \mathbf{z}_3\right\|_{\mathrm{F}}^2$$

$$+\frac{\beta}{2}\left\|\mathbf{G}_v\mathrm{vec}\,(\mathbf{G}_2) - \mathrm{vec}\,(\mathbf{G}_4) + \mathbf{z}_4\right\|_{\mathrm{F}}^2$$

$$+\frac{\beta}{2}\left\|\mathbf{x} - \mathrm{vec}\,(\mathbf{G}_5) + \mathbf{z}_5\right\|_{\mathrm{F}}^2. \tag{20}$$

Since $\mathbf{x}$ is the vectorization of $\mathbf{M}_k^{\mathrm{COSI}}$, when minimizing $L(\mathbf{x}, \mathbf{y}, \mathbf{z})$ to optimize the $\mathbf{M}_k^{\mathrm{COSI}}$, (20) can be rewritten as

$$\tilde{\mathbf{M}}_k^{\mathrm{COSI}} = \operatorname*{argmin}_{0 \le \mathbf{M}_k^{\mathrm{COSI}} \le 1} \frac{1}{2}\left\|\mathrm{vec}\,\left(\mathbf{M}_k^{\mathrm{COSI}}\right) - \mathrm{vec}\,\left(\boldsymbol{\theta}_k \odot \mathbf{T}_k^{\mathrm{FPSI}}\right)\right\|_{\mathrm{F}}^2$$

$$+\frac{\beta}{2}\left\|\mathrm{r}(\mathbf{D}_k)\mathrm{vec}\,\left(\mathbf{M}_k^{\mathrm{COSI}}\right) - \mathrm{vec}\,(\mathbf{G}_1) + \mathbf{z}_1\right\|_{\mathrm{F}}^2$$

$$+\frac{\beta}{2}\left\|\mathrm{vec}\,\left(\mathbf{M}_k^{\mathrm{COSI}}\right) - \mathrm{vec}\,(\mathbf{G}_2) + \mathbf{z}_2\right\|_{\mathrm{F}}^2$$

$$+\frac{\beta}{2}\left\|\mathrm{vec}\,\left(\mathbf{M}_k^{\mathrm{COSI}}\right) - \mathrm{vec}\,(\mathbf{G}_5) + \mathbf{z}_5\right\|_{\mathrm{F}}^2. \tag{21}$$

Taking the gradients $\mathbf{M}_k^{\mathrm{COSI}}$ and setting it equal to 0 leads to

$$\left((2\beta+1)\,\mathbf{I} + \beta\mathrm{r}(\mathbf{D}_k)^{\mathrm{T}}\mathrm{r}(\mathbf{D}_k)\right)\mathrm{vec}\left(\mathbf{M}_k^{\mathrm{COSI}}\right) = \mathrm{vec}\left(\boldsymbol{\theta}_k \odot \mathbf{T}_k^{\mathrm{FPSI}}\right)$$

$$+\beta\left(\mathrm{r}(\mathbf{D}_k)^{\mathrm{T}}\mathrm{vec}\,(\mathbf{G}_1) + \mathrm{vec}\,(\mathbf{G}_2)\right.$$

$$+\mathrm{vec}(\mathbf{G}_5) - \mathrm{r}(\mathbf{D}_k)^{\mathrm{T}}\mathbf{z}_1 - \mathbf{z}_2 - \mathbf{z}_5\bigg). \tag{22}$$

We solve (22) to obtain the solution $\mathbf{M}_k^{\mathrm{COSI}}$ and then introduce into (23) to produce the ideal thematic image of COSI $\tilde{\mathbf{M}}_k^{\mathrm{COSI}}$ for class k

$$\tilde{\mathbf{M}}_k^{\mathrm{COSI}} = \max\left(\mathbf{M}_k^{\mathrm{COSI}}, 0\right). \tag{23}$$

The optimization of $L(\mathbf{x}, \mathbf{y}, \mathbf{z})$ with respect to other variables $\mathbf{y}$ and $\mathbf{z}$ is described in Appendix B.

According to (8), after several alternate iterations for variables $\boldsymbol{\theta}_k$ and $\mathbf{M}_k^{\mathrm{COSI}}$, the final ideal thematic image of COSI for class k is derived. In this way, according to the steps of Algorithm 1, the ideal thematic images of COSI for all land-cover classes are produced. We assign the corresponding class labels to these ideal thematic images of COSI and then integrate them to obtain the final mapping result.

It can be found that using ADMM to control the variation factor can effectively identify the inaccurate spatiotemporal information of FPSI, i.e., when the inaccurate spatiotemporal information is generated in some areas of FPSI due to the large variation difference, the value of the corresponding variation factor will be reduced to reduce the inaccurate spatiotemporal information of this area to be input into the process of optimizing the ideal abundance images. On the contrary, when the spatial distribution of some areas of FPSI is very similar to that of COSI, the value of the corresponding variation factor will increase, so
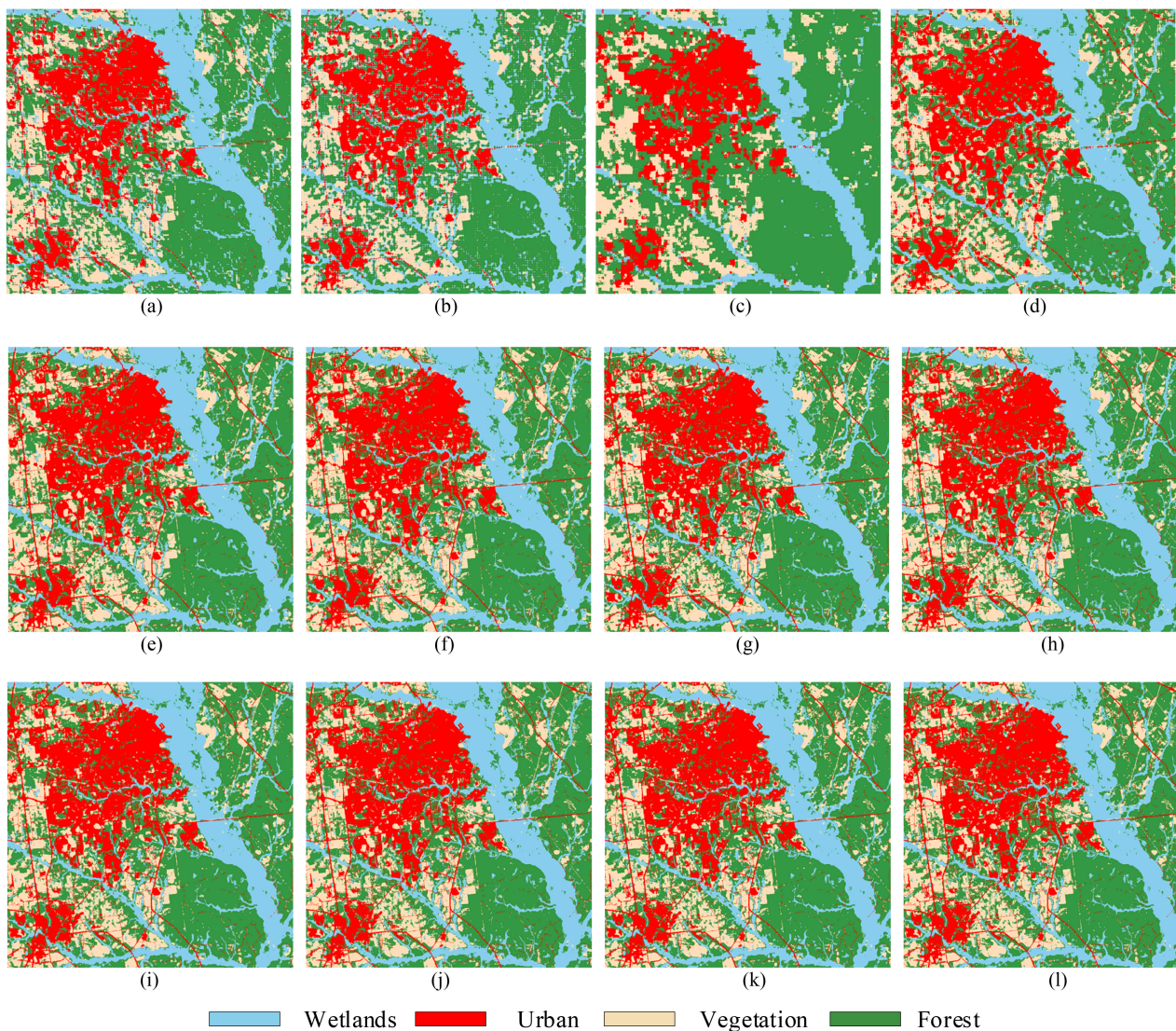
Fig. 6. Mapping results for NLCD 2011: SPM methods based on monotemporal image from (a)–(d): RBFI, NSAM, HNNP, and PSF. SSPM methods based on NLCD 2001 from (e)–(h): STD, SPSF, SMAP, and CVDBI. SSPM methods based on NLCD 2006 from (i)–(l): STD, SPSF, SMAP, and CVDBI.

TABLE I
EVALUATION INDICES OF MAPPING RESULTS FOR SYNTHETIC DATA SET 1

| Prior image	Method	Wetlands	Urban	Vegetation	Forest	OA	Kappa
No image	RBFI	85.48	74.90	66.62	80.46	77.76	0.6908
	NSAPM	87.27	74.11	67.27	82.47	78.88	0.7063
	HNNP	71.55	68.84	61.10	91.99	77.26	0.6734
	PSF	86.80	80.59	70.46	81.32	80.30	0.7262
NLCD 2001	STD	95.85	92.63	87.66	93.45	92.70	0.8986
	SPSF	96.93	94.45	90.17	94.86	94.34	0.9213
	SMAP	97.44	95.29	91.18	95.44	95.04	0.9310
	CVDBI	**98.21**	**96.83**	**93.43**	**96.64**	**96.41**	**0.9501**
NLCD 2006	STD	97.05	95.21	90.61	95.08	94.70	0.9262
	SPSF	98.14	96.72	92.87	96.37	96.17	0.9467
	SMAP	98.52	97.32	93.70	96.84	96.71	0.9543
	CVDBI	**99.19**	**98.40**	**95.61**	**97.83**	**97.82**	**0.9697**

Wetlands   Urban   Vegetation   Forest
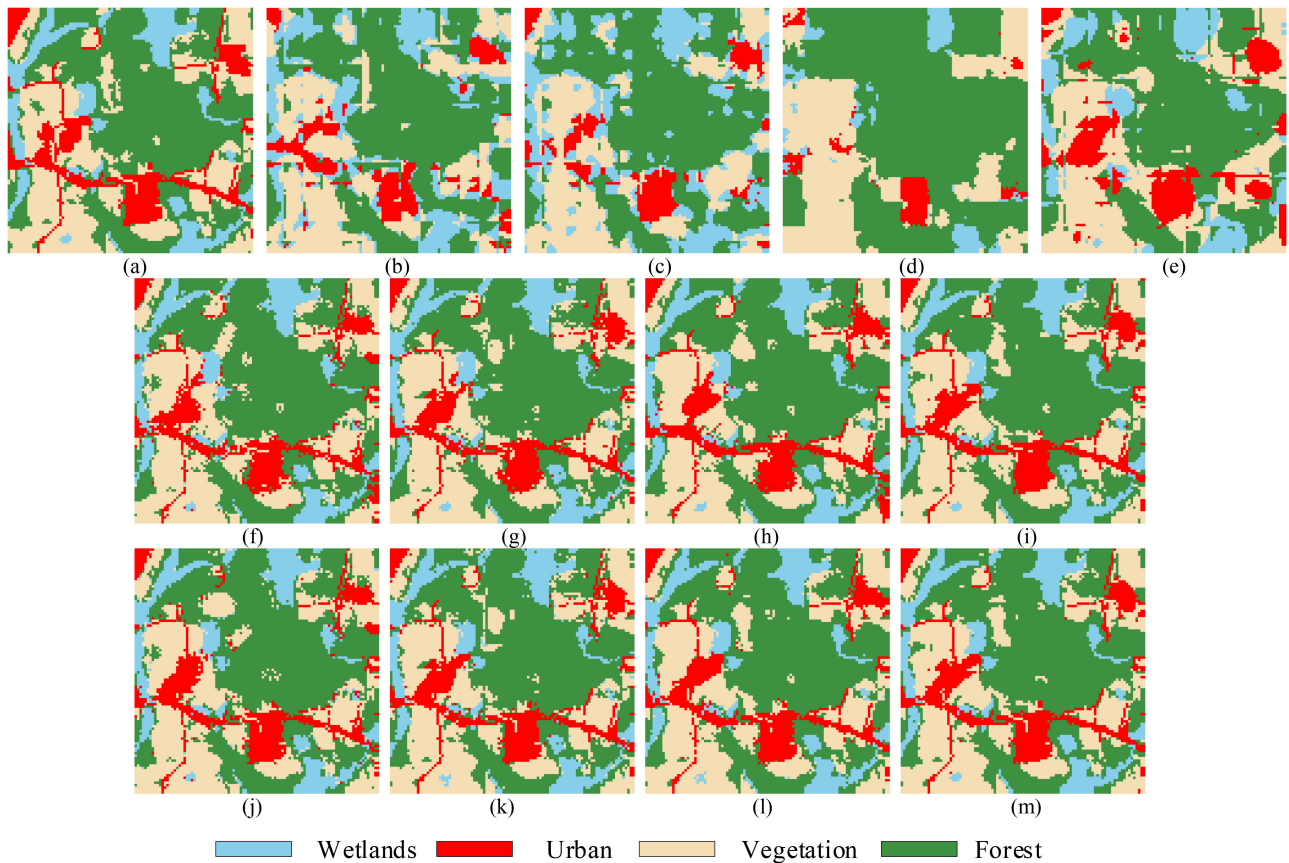
Fig. 7. Salient region from Fig. 6. (a) Reference image. SPM methods based on monotemporal image from (b)–(e): RBFI, NSAM, HNNP, and PSF. SSPM methods based on NLCD 2001 from (f)–(i): STD, SPSF, SMAP, and CVDBI. SSPM methods based on NLCD 2006 from (j)–(m): STD, SPSF, SMAP, and CVDBI.
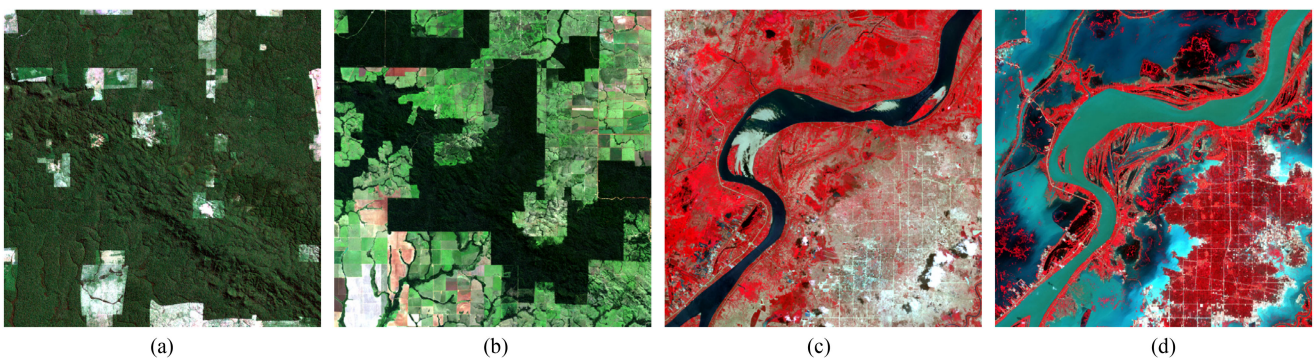

Fig. 8. Synthetic data set 2. (a) False color image of Amazon Rainforest in 1985 (bands 3, 2 and 1 for red, green, and blue). (b) False color image of Amazon Rainforest in 2013 (bands 4, 3, and 2 for red, green, and blue). (c) False color image of Mekong and Tonlé Sap Rivers before flood disaster (bands 5, 4, and 3 for red, green, and blue). (d) False color image of Mekong and Tonlé Sap Rivers after flood disaster (bands 5, 4, and 3 for red, green, and blue).

that this area can accurately assist the full use of spatiotemporal information, obtaining the better results.

III. EXPERIMENTS

Two synthetic experimental datasets and one real experimental dataset are used to qualitatively and quantitatively evaluate the performance of the proposed CVDBI. According to the general experimental process of SPM [18], to avoid the errors derived from the registration between images and spectral unmixing process, the input abundance images of COSI are generated by downsampling the reference classification image by a $S \times S$ linear mean filter, and the synthetic input abundance images of COSI are restored to the SPM result in the two synthetic experimental datasets. In contrast, to evaluate the performance of CVDBI on the uncertainty in a real situation, the real input
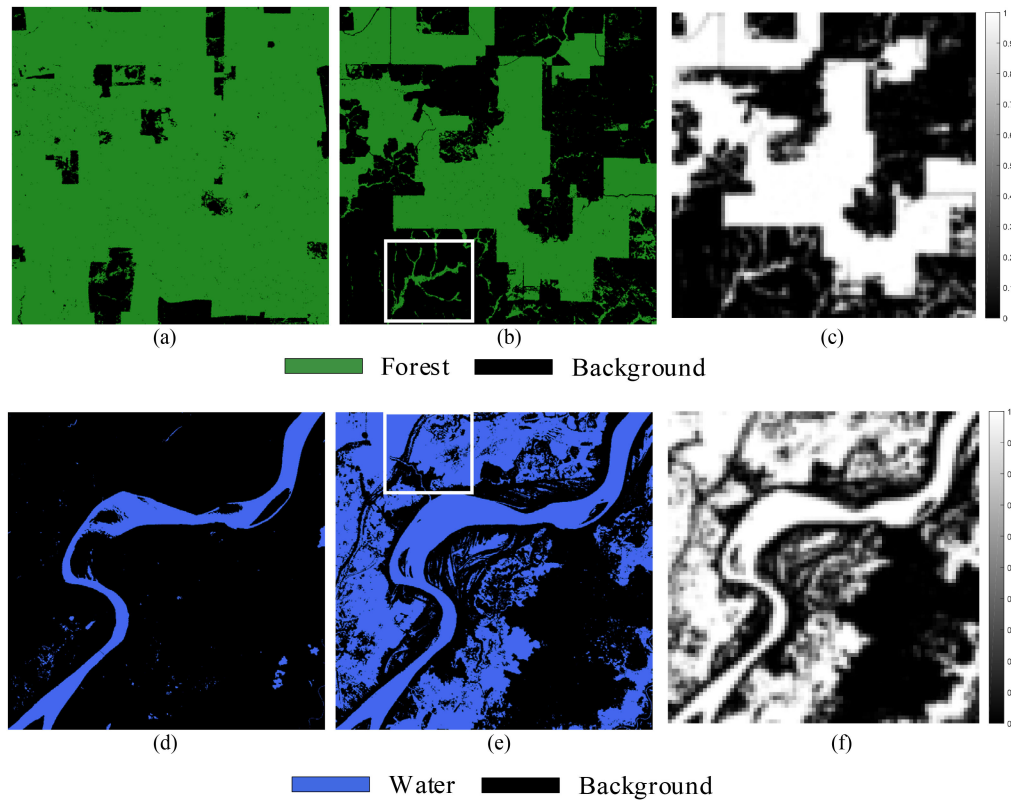
Fig. 9. (a) Reference classification image of Fig. 8(a). (b) Reference classification image of Fig. 8(b). (c) Abundance image of Fig. 8(b). (d) Reference classification image of Fig. 8(c). (e) Reference classification image of Fig. 8(d). (f) Abundance image of Fig. 8(d).

abundance images of COSI are derived from a real COSI by spectral unmixing based on least squares support vector machine (LSSVM) [10] in the real experimental dataset.

In CVDBI, a small value of λ_1 is selected to allow the variation factor $\boldsymbol{\theta}_k$ to adequately fit the experimental data, and a large value of λ_2 is set to have spectrally smooth variability. Therefore, the regularization parameters for the proposed CVDBI are empirically set at $\lambda_{\mathrm{M}} = 10^{-3}$, $\lambda_1 = 10^{-2}$, and $\lambda_2 = 10^3$. Nevertheless, the CVDBI still shows to be fairly insensitive to the choice of parameters, the detailed discussion will be given in Section IV-C. The alternating optimization process in Algorithm 1 is ran for at most 100 iterations or until the relative change of $\mathbf{M}_k^{\mathrm{COSI}}$ and $\boldsymbol{\theta}_k$ is less than 10^{-3}.

The proposed CVDBI is compared with the traditional SPM methods based on monotemporal image including SPM based on radial basis function interpolation (RBFI) [30], SPM based on new spatial attraction model (NSAM) [26], SPM based on Hopfield neural network with more prior information (HNNP) [29], and SPM based on reducing point spread function effect (PSF) [20], as well as the state-of-the-art SSPM methods including SSPM based on spatio-temporal dependence (STD) [12], SSPM based on point spread function effect (SPSF) [49], and SSPM based on MAP model (SMAP) [50]. The performances of the eight methods are evaluated based on the classification accuracy of each land-cover class, the overall accuracy (OA), and the Kappa coefficient (Kappa). All experiments are tested

by MATLAB 2018a software on a Pentium Dual-core Processor (2.20 GHz).

A. Synthetic Data Set 1

The synthetic data set 1 is used to evaluate the performance of the proposed CVDBI on FPSI captured at various times. As

TABLE II
EVALUATION INDICES OF MAPPING RESULTS FOR SYNTHETIC DATA SET 2

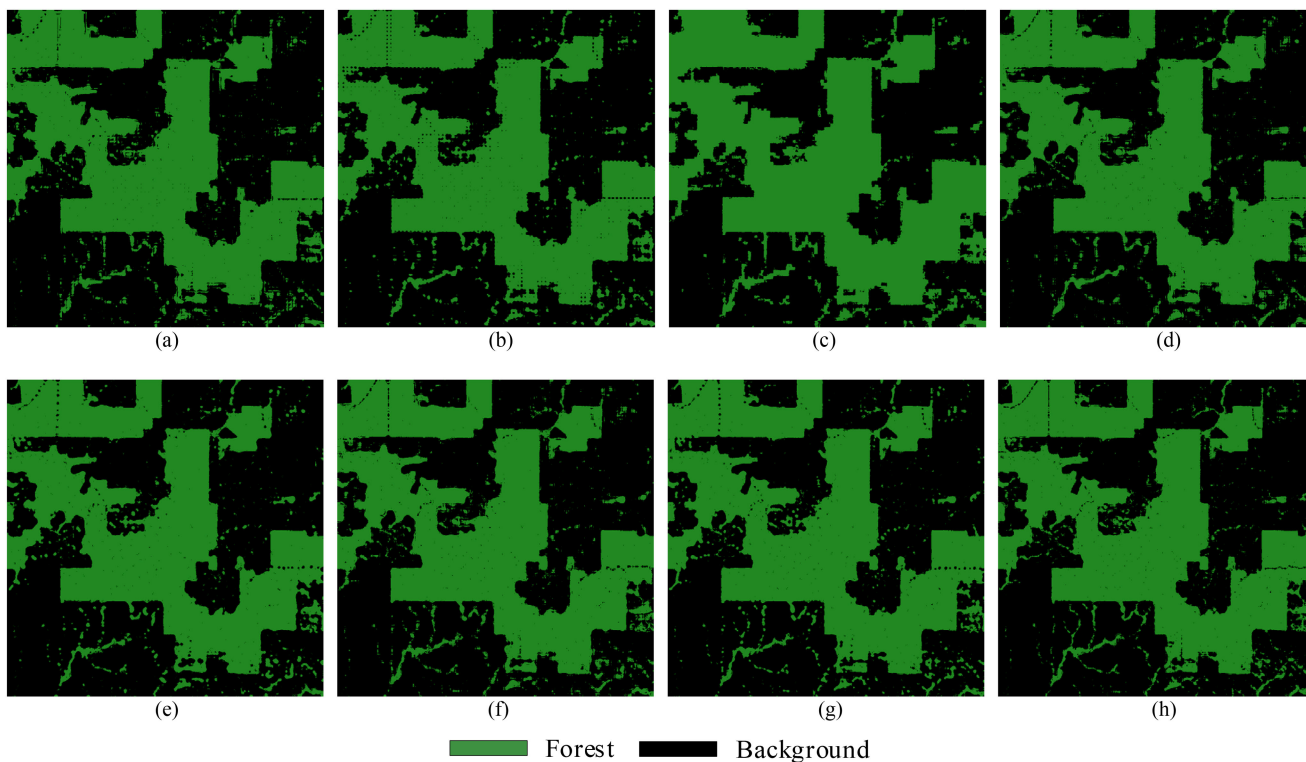| Amazon Rainforest				
Prior image	Method	PP	OA	Kappa
No image	RBFI	95.35	94.77	0.8938
	NSAPM	95.62	95.07	0.8999
	HNNP	91.84	94.21	0.8833
	PSF	95.63	95.15	0.9015
Landsat 5 in 1985	STD	95.74	95.21	0.9028
	SPSF	96.09	95.60	0.9106
	SMAP	96.21	95.74	0.9136
	CVDBI	**97.05**	**96.68**	**0.9326**
Mekong and Tonlé Sap Rivers				
Prior image	Method	PP	OA	Kappa
No image	RBFI	89.54	89.18	0.7834
	NSAPM	90.06	89.72	0.7942
	HNNP	81.51	88.76	0.7761
	PSF	90.68	90.31	0.8059
Landsat 8 before flood disaster	STD	90.84	90.71	0.8080
	SPSF	91.27	90.93	0.8184
	SMAP	91.70	91.42	0.8281
	CVDBI	**93.41**	**93.16**	**0.8630**

Fig. 10. Mapping results for Amazon Rainforest: SPM methods based on monotemporal image from (a)–(d): RBFI, NSAM, HNNP, and PSF. SSPM methods based on Landsat 5 in 1985 from (e)–(h): STD, SPSF, SMAP, and CVDBI.

Fig. 11. Salient region from Fig. 10. (a) Reference image. SPM methods based on monotemporal image from (b)–(e): RBFI, NSAM, HNNP, and PSF. SSPM methods based on Landsat 5 in 1985 from (f)– (i): STD, SPSF, SMAP, and CVDBI.

shown in Fig. 4, the synthetic data set 1 from National Land-Cover Database (NLCD) includes three maps with 30-m spatial resolution, 1000×1000 pixels and 4 land-cover classes (i.e., Wetlands, Urban, Vegetation, and Forest), which are collected over Georgia, U.S. in 2001, 2006, and 2011, respectively. Since the three maps are obtained by classification based on raster

method [13], they are considered as the reference classification images. We perform the experiments twice to test the performance of CVDBI on FPSI captured at various times, the NLCD 2001 image in Fig. 4(a) and the NLCD 2006 image in Fig. 4(b) are selected as FPSI, respectively. Because the NLCD 2001 image and NLCD 2006 image have been classified, they could

Fig. 12.   Mapping results for Mekong and Tonlé Sap Rivers: SPM methods based on monotemporal image from (a)–(d): RBFI, NSAM, HNNP, and PSF. SSPM methods based on Landsat 8 before flood disaster from (e)–(h): STD, SPSF, SMAP, and CVDBI.
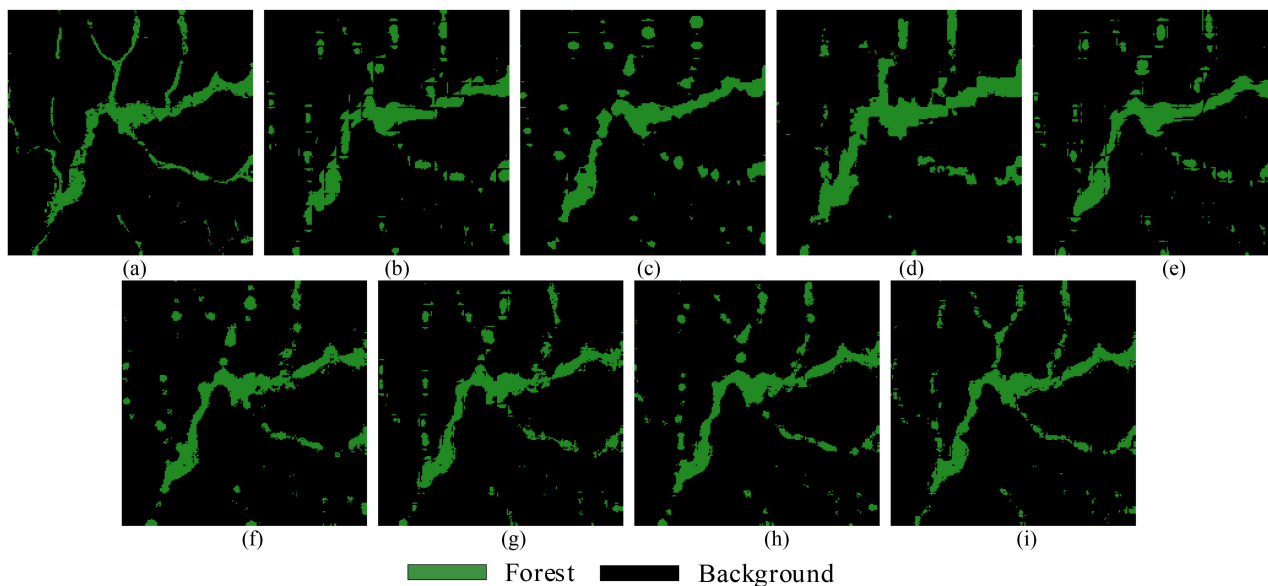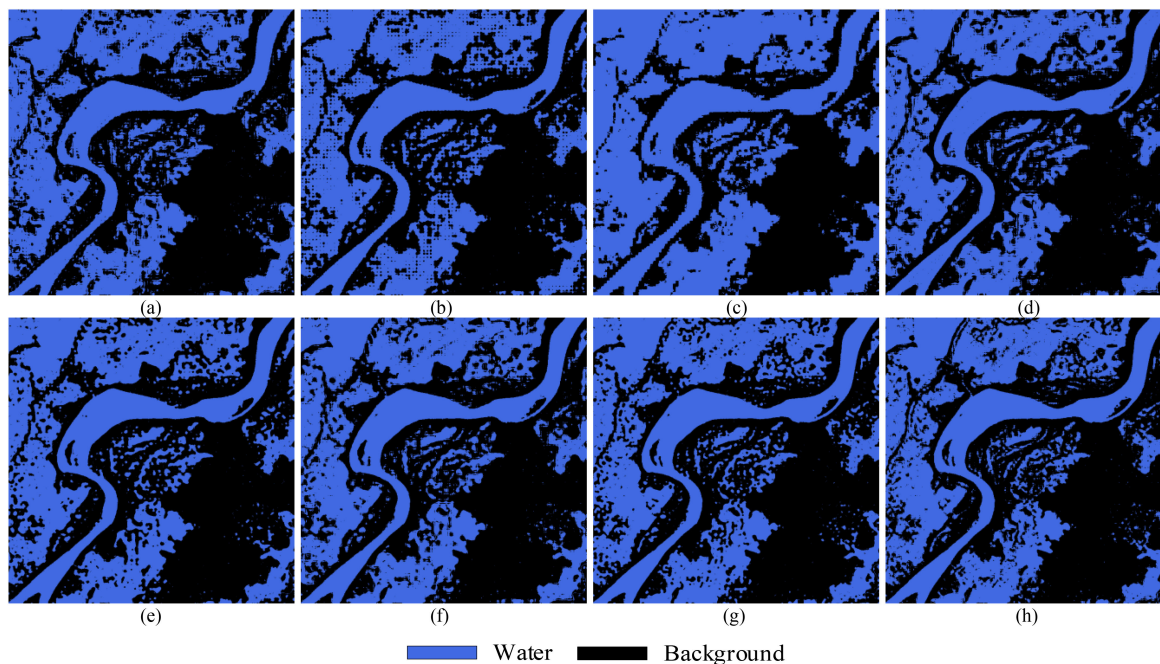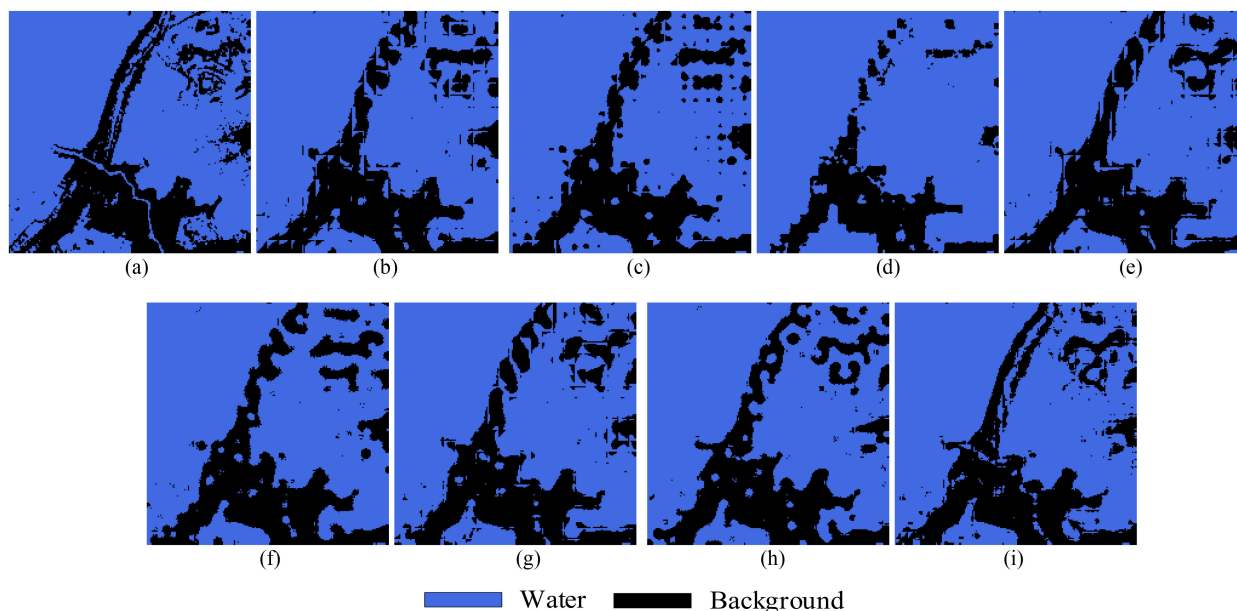

Fig. 13.   Salient region from Fig. 12. (a) Reference image. SPM methods based on monotemporal image from (b)–(e): RBFI, NSAM, HNNP, and PSF. SSPM methods based on Landsat 8 before flood disaster from (f)–(i): STD, SPSF, SMAP, and CVDBI.

directly provide the fine thematic images of FPSI. The NLCD 2011 image in Fig. 4(c) considered as COSI is downsampled by a 8×8 mean filter to produce the synthetic input abundance images of COSI with a 240-m spatial resolution, which are shown in Fig. 5. Although the coarse abundance images of COSI could provide the proportion information of the mixed pixels belonging to land-cover classes, the specific spatial distribution information of land-cover classes is uncertain in these abundance

images. Thus, SPM is proposed to handle the abundance images to obtain the mapping result with the specific spatial distribution information of land-cover classes.

The mapping results of the eight SPM methods for NLCD 2011 are shown in Fig. 6. In order to facilitate observation, as shown in Fig. 7, a salient subregion of the mapping results with 100×100 pixels marked in Fig. 4(c) with a black frame are magnified. Comparing with the reference image in Fig. 7(a), the
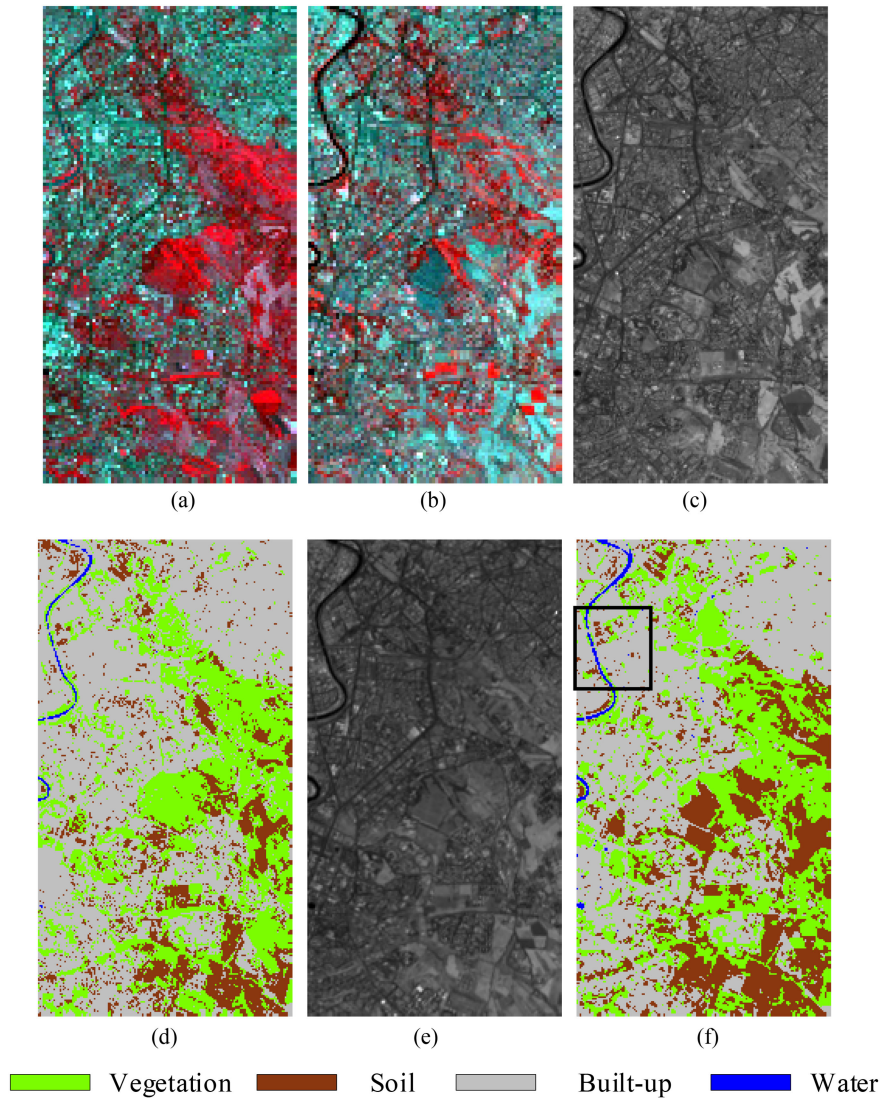
Fig. 14.   Real dataset. (a) False color image of Landsat 8 in 2014 (bands 5, 2, and 3 for red, green, and blue). (b) False color image of Hyperion in 2002 (bands 150, 10, and 24 for red, green, and blue). (c) Panchromatic image of Landsat 8 in 2014. (d) Reference classification image of Fig. 14(c). (c) Panchromatic image of Landsat 8 in 2002. (d) Reference classification image of Fig. 14(e).

TABLE III
EVALUATION INDICES OF MAPPING RESULTS FOR REAL DATASET

Prior image	Method	Vegetation	Soil	Built-up	Water	OA	Kappa
No image	RBFI	79.84	69.97	86.68	61.03	80.92	0.6962
	NSAPM	79.99	70.00	86.72	73.85	81.09	0.6990
	HNNP	59.34	68.72	96.15	82.56	79.91	0.6674
	PSF	80.03	76.69	88.16	61.05	83.19	0.7335
Landsat 8 in 2014	STD	88.92	83.15	92.46	83.59	89.37	0.8308
	SPSF	90.46	86.03	93.38	83.33	91.01	0.8570
	SMAP	91.19	88.84	94.29	81.03	92.14	0.8752
	CVDBI	**93.08**	**91.69**	**96.41**	**88.23**	**93.89**	**0.9088**

mapping results of the four traditional SPM methods based on monotemporal image from Fig. 7(b)–(e) are far away from ideal. For example, there are many boundaries of protruding burrs in Forest class and areas of disconnected shapes in Urban class, which was because these methods lack *a priori* knowledge of the actual geographical distribution to constrain the fuzziness

and uncertainty of the mapping results. With the help of the auxiliary spatiotemporal information provided by NLCD 2001 or NLCD 2006, the abovementioned phenomenon is alleviated in the mapping results of SSPM in Fig. 7(f)–(i) or (j)–(m). Since the proposed CVDBI takes into account the variation difference between COSI and FPSI, when using the same FPSI,

Fig. 15. Mapping results for real dataset: SPM methods based on monotemporal image from (a)–(d): RBFI, NSAM, HNNP, and PSF. SSPM methods based on Landsat 8 in 2014 (e)–(h): STD, SPSF, SMAP, and CVDBI.

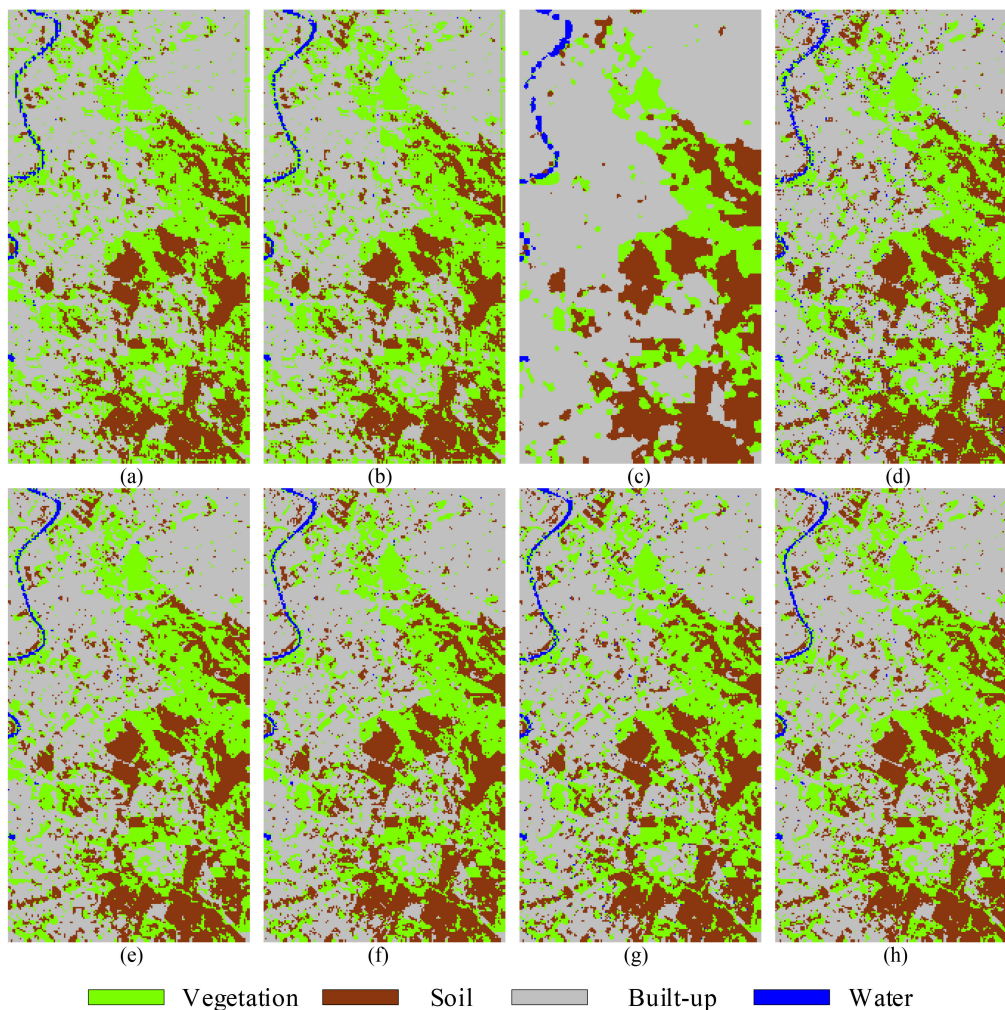there are smoother boundaries and more continuous areas in Fig. 7(i) and (m) than those in Fig. 7(f)–(h) or (j)–(l). Thus, the mapping result of CVDBI is closer to the reference image than that of the other SSPM methods. This proves that CVDBI can perform best in the case of using FPSI captured at various times.

In addition to visual comparison, Table I shows the three evaluation indices of mapping result including the classification accuracy of each land-cover class (%), OA (%), and Kappa. The traditional SPM methods based on monotemporal image could consider that there is unchanged land cover affect. The SSPM methods could consider that there is changed land cover affect. As shown in Table I, we can see that even with the changed land cover affect, SSPM methods can still obtain the higher evaluation indicators than traditional SPM methods. In addition, the proposed CVDBI performs better than the other seven SPM methods. For instance, when using NLCD 2001 as FPSI, compared with the classification accuracy of each land-cover class (%) and OA (%) in the SMAP, the accuracy of Wetlands, Urban, Vegetation, Forest, and OA (%) in CVDBI increased by about 0.77, 1.54, 2.25, 1.20, and 1.37 percentage,

respectively. According to the definition of OA (%), because there are 1000×1000 pixels in the tested imagery, an increase of 1.37% means that the mapping result of the CVDBI produces 13 700 more correct mapping pixels than that of SMAP, which represents a significant improvement.

In addition, this experiment is also be utilized to analyze the performance of the proposed method for the different change rates. As shown in Table I, for each SSPM method, it is worth noting that the value of the evaluation indices by using NLCD 2001 as FPSI is lower than that by using NLCD 2006 as FPSI. This is because NLCD 2001 is farther away from the collection time of NLCD 2011 than NLCD 2006, the land cover change rate between NLCD 2001 and NLCD 2011 is more obvious. This experimental result also proves that the land cover change rate between COSI and FPSI does affect the performance of SSPM methods, and the greater land cover change rate results in the more serious influence. Therefore, the lower rates of changed land cover affect for SSPM methods could produce the better mapping results. The CVDBI obtains the higher OA (%) of 84.82%, and Kappa of 0.7027 by using NLCD 2006 as FPSI than that by using NLCD 2001 as FPSI. When using the same

FPSI captured at various times, the proposed CVDBI always has the highest OA (%) and Kappa. This proves that CVDBI could show the ideal performance by using the FPSI captured at various times to relieve the limitations of the close acquisition time of COSI and FPSI in the current SSPM methods.

B. Synthetic Data Set 2

We test the synthetic data set 2 including two sets of four multispectral images. It turns out that CVDBI could be effectively applied to some large variation difference scenes where the time interval of collecting between COSI and FPSI is long, or the frequency of disaster change between COSI and FPSI is high. As shown in Fig. 8(a) and (b), the first set of two multispectral images with 30-m spatial resolution, 800×800 pixels and 2 land-cover classes (i.e., Forest and Background) are collected over Amazon Rainforest in Brazil. The study area is mainly covered by forest in Fig. 8(a) collected by Landsat 5 imager in 1985. Due to the long-term human destruction, forest has been seriously reduced in Fig. 8(b) collected by Landsat 8 imager in 2013. Therefore, there is a large variation difference between Fig. 8(a) and (b) due to a long-time interval of collecting. Fig. 8(a) and (b) is selected as FPSI and COSI, respectively, to test the performance of CVDBI on the scene where the time interval of collecting between COSI and FPSI is very long.

As shown in Fig. 8(c) and (d), the second set of two multispectral images with 30-m spatial resolution, 800×800 pixels and 2 land-cover classes (i.e., Water and Background) are acquired along the Mekong and Tonlé Sap Rivers in Cambodia. Fig. 8(c) is acquired by Landsat 8 before flood disaster on May 17, 2013. However, in October, the heavy seasonal rains cause the flood along the Mekong and Tonlé Sap Rivers, a Landsat 8 image shown in Fig. 8(d) is acquired after flood disaster on 24 October 2013. Thus, there is a large variation difference between Fig. 8(c) and (d) due to a high frequency of disaster change. Fig. 8(c) and (d) is selected as FPSI and COSI, respectively, to test the performance of CVDBI on the scene where the frequency of disaster change between COSI and FPSI is high.

For Amazon Rainforest data, as shown in Fig. 9(a) and (b), we use the classification method based on support vector machine (SVM) by ENVI software to classify Fig. 8(a) and (b) to obtain their reference classification images. Fig. 9(a) provides the fine thematic image of FPSI for Forest class. Fig. 9(b) provides the reference image of the mapping results and then is downsampled by a 8×8 mean filter to produce the synthetic input abundance image of COSI with a 240-m spatial resolution [as shown in Fig. 9(c)]. For Mekong and Tonlé Sap Rivers data, we utilize the same classification method to obtain Fig. 9(d) as the fine thematic image of FPSI for Water class, and Fig. 9(e) as the reference image of the mapping results. We also apply the same 8×8 mean filter to Fig. 9(e) to produce Fig. 9(f) as the synthetic input abundance image of COSI.

For the experiment of Amazon Rainforest, Fig. 10(a)–(d) shows the mapping results of four SPM methods based on monotemporal image and Fig. 10(e)–(h) shows the mapping results of four SSPM methods based on Landsat 5 in 1985. It is noted that Fig. 10(e)–(h) is closer to the reference image

in Fig. 9(b) than Fig. 10(a)–(d) due to the prior auxiliary spatiotemporal information from Landsat 5. As shown in Fig. 11, a salient subregion of the mapping results with 200×200 pixels marked in Fig. 9(b) with a white frame is magnified to facilitate observation. Comparing with the reference image in Fig. 11(a), we could find that the Forest class is not continuous, and some small areas are hardly mapped by using the three existing SSPM methods (i.e., STD, SPSF, and SMAP) in Fig. 10(f)–(h). This is because the existing SSPM methods do not effectively identify the inaccurate spatiotemporal information of the FPSI. Especially, when there is a large variation difference between COSI and FPSI due to the difference of nearly 30 years of capture time, FPSI may provide wrong auxiliary information, resulting in the unsatisfactory mapping result. In contrary, the proposed CVDBI effectively identifies the inaccurate spatiotemporal information of the FPSI, these phenomena are alleviated in Fig. 11(i).

For the experiment of Mekong and Tonlé Sap Rivers, the mapping results of eight SPM methods are shown in Fig. 12. And a salient subregion of the mapping results with 200×200 pixels marked in Fig. 9(e) with a white frame is magnified to show in Fig. 13. Similar to the experimental results of Amazon Forest, when there is a large variation difference between COSI and FPSI due to the high frequency of disaster change, the mapping result of the CVDBI is the closest to the reference image among all the obtained mapping results.

For the binary classification problem, we use producer accuracy (PA) (%), OA (%), and Kappa as the evaluation indices. The definition of PA (%) is that the ratio of the number of pixels correctly classified as Class A in mapping result to the number of pixels of Class A in the real case in reference image. PA (%), OA (%), and Kappa of the eight methods for the two experimental data are given in Table II, where it can be seen that the proposed CVDBI had the highest PA (%) of 97.05%, OA (%) of 96.68%, and Kappa of 0.9326 for Amazon Rainforest, and the highest PA (%) of 93.41%, OA (%) of 93.16%, and Kappa of 0.8630 for Mekong and Tonlé Sap Rivers. Therefore, when there is a large variation difference between COSI and FPSI, the proposed CVDBI performs better than other methods.

C. Real Dataset

In a practice situation, the real input abundance images are derived from the spectral unmixing of COSI, and some uncertainty, such as the registration error between COSI and FPSI, the spectral unmixing error of abundance images and the classification error of reference image, exists in the experimental process. To further evaluate the effectiveness of the proposed CVDBI, a real dataset are tested in experiment 3.

Fig. 14(a) and (b) have 308×164 pixels and 4 land-cover classes (i.e., vegetation, soil, built-up, and water), which cover an area in Rome, Italy. As shown in Fig. 14(a), a multispectral image selected as FPSI with 8 spectral bands of 30-m spatial resolution and 1 panchromatic band of 15-m spatial resolution is obtained by Landsat 8 imager in 2014. As shown in Fig. 14(b), a hyperspectral image selected as COSI with 198 spectral bands of 30-m spatial resolution is obtained by Hyperion imaging spectrometer from Earth Observing-1 in 2002.
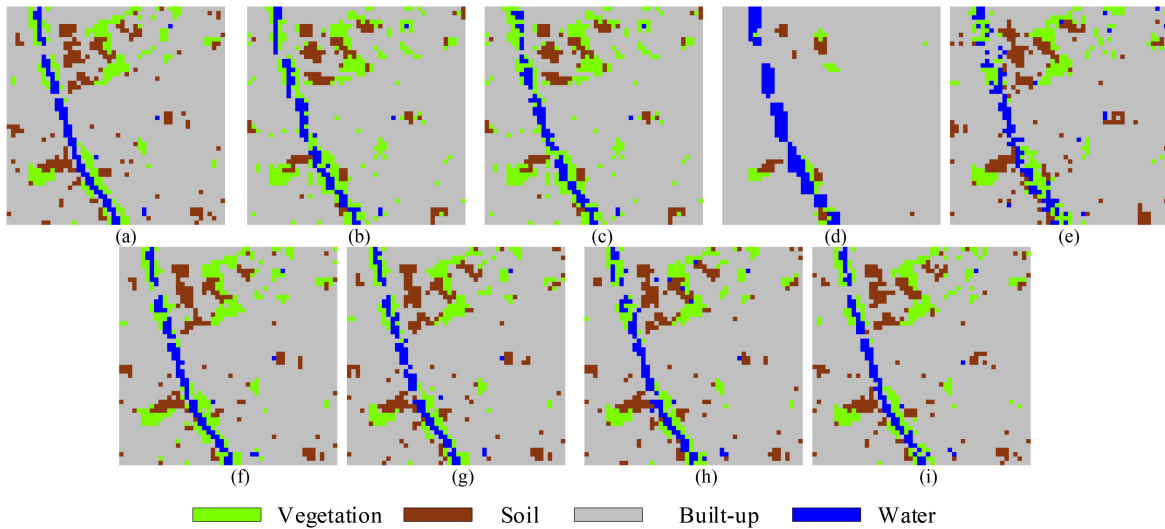
Fig. 16.   Salient region from Fig. 15. (a) Reference image. SPM methods based on monotemporal image from (b)–(e): RBFI, NSAM, HNNP, and PSF. SSPM methods based on Landsat 8 before flood disaster from (f)–(i): STD, SPSF, SMAP, and CVDBI.
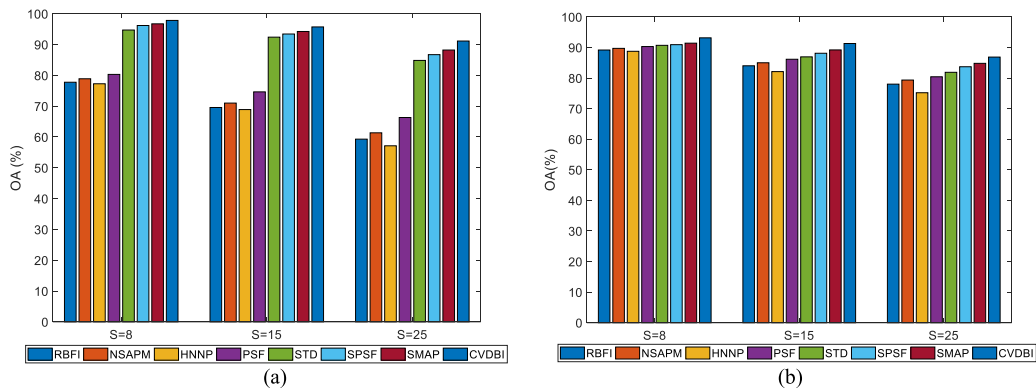

Fig. 17.   OA (%) of the eight SPM methods in relation to different scale factors S (a) in experiment 1 and (b) in experiment 2.

The panchromatic band of 15-m spatial resolution from Fig. 14(a) selected as FPSI is shown in Fig. 14(c). As shown in Fig. 14(d), we still use the classification method based on SVM to classify Fig. 14(c) to yield the reference classification image as the fine thematic images of FPSI. The input abundance images of COSI are obtained by unmixing the Fig. 14(b) with 30-m spatial resolution. Thus, the scale factor S between PFSI and COSI was 2. In addition, to obtain the reference image of the mapping results with 15-m spatial resolution, another panchromatic band of 15-m spatial resolution from Landsat 8 in 2002 having the same capture time and area as Fig. 14(b) is utilized and shown in Fig. 14(e). Fig. 14(e) is also classified to produce the reference image shown in Fig. 14(f) by the classification method based on SVM.

Fig. 15 shows the mapping results of the eight methods for real dataset. Similarly, for visual comparison purposes, a salient sub-region of the mapping results with 50×50 pixels marked in Fig. 14(f) with a black frame is magnified in Fig. 16. Comparing with the reference image, similar to Experiments 1 and 2, the proposed CVDBI achieves the more continuous and smoother
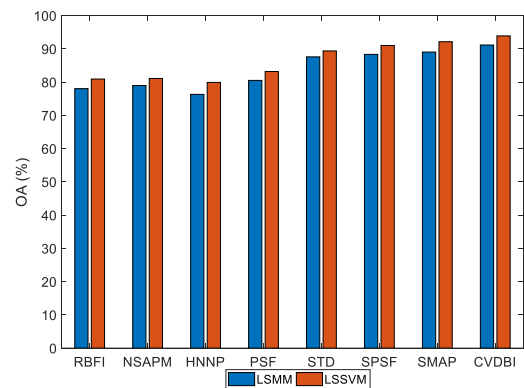

Fig. 18.   OA (%) of the eight SPM methods in relation to two spectral unmixing methods in Experiment 3.

mapping result than the other seven methods. Table III lists the three evaluation indices of the eight SPM methods, where it can also be seen that the proposed CVDBI outperforms the other seven methods, and obtains the highest values of the three
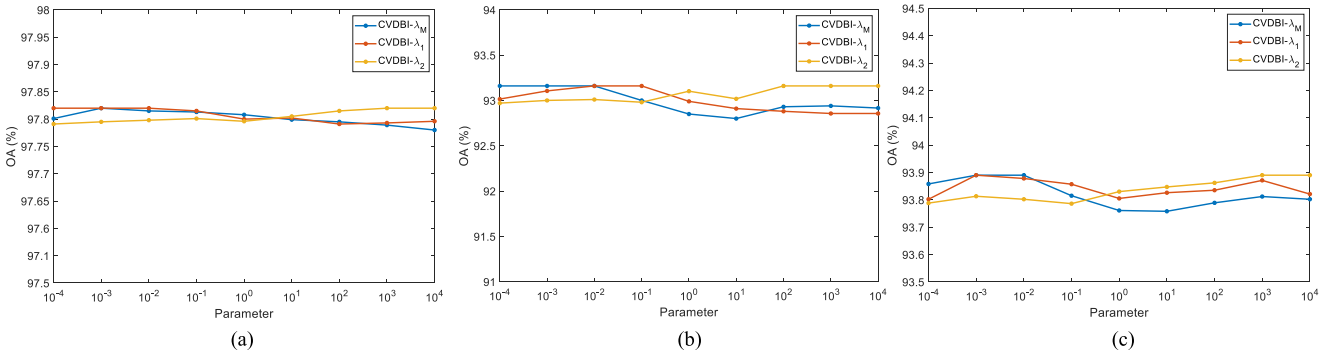
Fig. 19.   OA (%) of the CVDBI in relation to parameters sensitivity (a) in experiment 1, (b) in experiment 2, and (c) in experiment 3.
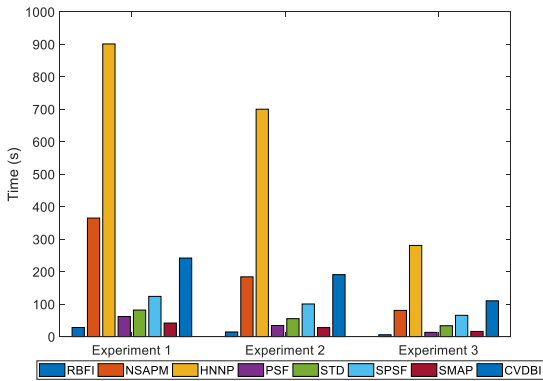

Fig. 20.   Processing time of the eight SPM methods in the three experiments.

evaluation indices. Therefore, in practice, the proposed CVDBI could achieve good performance due to effectively identifying the inaccurate spatiotemporal information of the FPSI.

IV. DISCUSSION

A. Scale Factor

In experiments 1 and 2, the synthetic input abundance images of COSI are obtained by downsampling the reference classification image by a scale factor $S \times S$ mean filter. Different values of S mean that the abundance images of COSI with different resolution are produced. Thus, the performance of the proposed CVDBI under the influences of different values of the scale factor S is discussed here. The eight SPM methods are tested by repeating Experiments 1 (NLCD 2006 as FPSI) and 2 (Mekong and Tonlé Sap Rivers) for three values of the scale factor S (i.e., 8, 15, and 25).

Fig. 17 shows the OA (%) values of the eight SPM methods at different scale factors S in experiments 1 and 2. Since the higher value of S indicates the coarser input abundance images, the OA (%) of the eight methods all decreases with S, but the proposed CVDBI still obtained the highest OA (%) value among all the methods in all the three scale factors. Therefore, the proposed CVDBI has good performance and certain stability under the influences of different values of the scale factor S.

B. Spectral Unmixing

In experiment 3, the real input abundance images of COSI are obtained by spectral unmixing based on LSSVM. However, the error caused by spectral unmixing will affect the mapping result. Therefore, it is necessary to discuss the performance of the proposed CVDBI under the influences of different spectral unmixing. Spectral unmixing based on linear spectral mixture model (LSMM) [53] is selected to replace LSSVM in Experiment 3 to obtain the input abundance images.

The OA (%) values of the eight SPM methods in relation to two spectral unmixing methods in Experiment 3 are shown in Fig. 18. Since LSMM is not more effective than LSSVM [10], the OA (%) of the eight SPM methods decreases when using LSMM. Thus, a more effective spectral unmixing method will produce less spectral unmixing error, resulting in the higher OA (%). However, no matter which spectral unmixing method is used, the proposed CVDBI always achieves the highest OA (%). The experimental results show that the CVDBI is more robust to the choice of spectral unmixing than other SPM methods

C. Parameter Sensitivity

The sensitivity of the proposed CVDBI for λ_M, λ_1, and λ_2 is explored in Experiments 1 (NLCD 2006 as FPSI), 2 (Mekong and Tonlé Sap Rivers), and 3. For the experimental setup, each parameter is varied in the range of $[10^{-4}, 10^4]$ at an interval of 10 times, while keeping the remaining ones fixed at the values described in Section III. In other words, each experiment only changes the value of one parameter, and the values of the other two parameters remain unchanged.

As shown in Fig. 19, we compute the OA (%) by the CVDBI, and the experimental results clearly show that even if the parameter value changes in different orders of magnitude, it will only have a relatively small impact on the resulting OA (%). Therefore, the performance of the proposed method is not overly sensitive to the choice of parameters.

D. Running Time

The running time is also an important index to evaluate the performance of the SPM. The running time of eight SPM methods in Experiments 1 (NLCD 2006 as FPSI), 2 (Mekong and

Tonlé Sap Rivers), and 3 is recorded in Fig. 20. Observing from the results, when comparing with the other three SSPM methods (i.e., STD, SPSF, and SMAP), the proposed CVDBI requires the more time to obtain the final mapping result. The main reason is that the CVDBI utilizes ADMM to update the variables $\boldsymbol{\theta}_k$ and $\mathbf{M}_k^{\text{COSI}}$ by alternate iterations. Thus, the proposed CVDBI is to obtain the ideal mapping result at the cost of longer running time.

V. CONCLUSION

With the help of spatiotemporal information from PFSI, SSPM performers better than the traditional SPM based on monotemporal image. However, the current SSPM methods rarely identify the inaccurate spatiotemporal information of the FPSI, affecting the accuracy of the mapping result. In this article, a SSPM based on variation difference between images (CVDBI) is proposed to solve the abovementioned problem. CVDBI first obtains the coarse abundance images of COSI by unmixing COSI and the fine thematic images of FPSI by classifying FPSI. DOM and variation difference observation mode are then established. Next, a separable convex optimization model is proposed by integrating DOM and VDOM to optimize the variation difference factor and the ideal thematic image of COSI. Finally, we use the ADMM to solve the separable convex optimization problem to derive the mapping result. Experiments on three datasets are performed to validate the proposed CVDBI. The proposed method is compared to the traditional SPM methods, as well as the SSPM methods. The conclusions are as follows.

1) The proposed CVDBI provides an effective solution by identifying the inaccurate spatiotemporal information of the FPSI. From both visual comparison and index evaluation, the CVDBI can produce more accurate mapping result than the current SSPM methods.
2) The proposed CVDBI could relieve the limitations of the close acquisition time of COSI and FPSI in the current SSPM methods. From the results in Experiment 1, CVDBI show a better performance than the other SSPM methods in the case of using FPSI captured at various times.
3) The proposed CVDBI is applicable to a large variation difference between COSI and FPSI. From the results in Experiment 2, the CVDBI always obtain the best result when there is a long-time interval of collecting between COSI and FPSI, or a high frequency of disaster change between COSI and FPSI.
4) The proposed CVDBI can achieve good performance in the real situation. From the results in Experiment 3, when there are some uncertainties in the situation, the proposed CVDBI also performs better than other SSPM methods.

With the rapid development of remote sensing technology, it is not very difficult to obtain FPSI at other times. As long as there is FPSI, we can get the ideal thematic images through classification method. Of course, when there is no ideal thematic image, the proposed CVDBI will be affected. This is a limiting condition for CVDBI. We will improve the CVDBI in the future so that it can obtain better results without using ideal thematic images.

APPENDIX A

In this section, the optimization of the scaled augmented Lagrange $L(\boldsymbol{\theta}_k, \mathbf{G}, \mathbf{z})$ in (12) with respect to the other variables $\mathbf{G}$ and $\mathbf{z}$ is described.

A. Optimizing $\mathbf{G}$

We write the optimization problem for $\mathbf{G}$ as

$$\mathbf{G} = \underset{0 \leq \mathbf{G} \leq 1}{\operatorname{argmin}} \frac{1}{2} \left\| \mathbf{M}_k^{\text{COSI}} - \mathbf{G} \right\|_{\text{F}}^2 + \frac{\beta}{2} \left\| -\boldsymbol{\theta}_k \odot \mathbf{T}_k^{\text{FPSI}} + \mathbf{G} + \mathbf{z} \right\|_{\text{F}}^2. \tag{24}$$

We take the derivative with respect to $\mathbf{G}$ and set it equal to zero as

$$\left(1 - \frac{1}{\beta}\right) \mathbf{G} = \boldsymbol{\theta}_k \odot \mathbf{T}_k^{\text{FPSI}} - \mathbf{z} - \frac{1}{\beta} \mathbf{M}_k^{\text{COSI}}. \tag{25}$$

Equation (22) could be solved to obtain the solution of $\mathbf{G}$.

B. Optimizing $\mathbf{z}$

The alternate update is defined as

$$\mathbf{z} \leftarrow \mathbf{z} + \mathbf{G} - \boldsymbol{\theta}_k \odot \mathbf{T}_k^{\text{FPSI}}. \tag{26}$$

APPENDIX B

In this section, we introduce the optimization of the scaled augmented Lagrange $L(\mathbf{x}, \mathbf{y}, \mathbf{z})$ in (20) with respect to the other variables $\mathbf{y}$ and $\mathbf{z}$.

A. Optimizing $\mathbf{G}_1$

The subproblem for $\mathbf{G}_1$ can be written as

$$\mathbf{G}_1 = \underset{0 \leq \mathbf{G}_1 \leq 1}{\operatorname{argmin}} \frac{1}{2} \left\| \operatorname{vec}\left(\mathbf{A}_k^{\text{COSI}}\right) - \operatorname{vec}\left(\mathbf{G}_1\right) \right\|_{\text{F}}^2$$
$$+ \frac{\beta}{2} \left\| \operatorname{r}(\mathbf{D}_k)\operatorname{vec}\left(\mathbf{M}_k^{\text{COSI}}\right) - \operatorname{vec}\left(\mathbf{G}_1\right) + \mathbf{z}_1 \right\|_{\text{F}}^2. \tag{27}$$

Taking the derivative of $\mathbf{G}_1$ and setting it equal to zero, we obtain (28). We solve (28) to derive $\mathbf{G}_1$

$$(1+\beta) \operatorname{vec}\left(\mathbf{G}_1\right) = \operatorname{vec}\left(\mathbf{A}_k^{\text{COSI}}\right) + \beta \operatorname{r}(\mathbf{D}_k)\operatorname{vec}\left(\mathbf{M}_k^{\text{COSI}}\right) + \beta \mathbf{z}_1. \tag{28}$$

B. Optimizing $\mathbf{G}_2$

The subproblem for $\mathbf{G}_2$ can be written as

$$\mathbf{G}_2 = \underset{0 \leq \mathbf{G}_2 \leq 1}{\operatorname{argmin}} \frac{\beta}{2} \left\| \operatorname{vec}\left(\mathbf{M}_k^{\text{COSI}}\right) - \operatorname{vec}\left(\mathbf{G}_2\right) + \mathbf{z}_2 \right\|_{\text{F}}^2$$
$$+ \frac{\beta}{2} \left\| \mathbf{G}_h \operatorname{vec}\left(\mathbf{G}_2\right) - \operatorname{vec}\left(\mathbf{G}_3\right) + \mathbf{z}_3 \right\|_{\text{F}}^2$$
$$+ \frac{\beta}{2} \left\| \mathbf{G}_v \operatorname{vec}\left(\mathbf{G}_2\right) - \operatorname{vec}\left(\mathbf{G}_4\right) + \mathbf{z}_4 \right\|_{\text{F}}^2. \tag{29}$$

We also take the derivative of $\mathbf{G}_2$ and set it equal to zero as

$$\left(\mathbf{I} + \mathbf{G}_h^{\text{T}}\mathbf{G}_h + \mathbf{G}_v^{\text{T}}\mathbf{G}_v\right) \operatorname{vec}\left(\mathbf{G}_2\right) = \operatorname{vec}\left(\mathbf{M}_k^{\text{COSI}}\right)$$
$$+ \mathbf{G}_h^{\text{T}} \operatorname{vec}\left(\mathbf{G}_3\right) + \mathbf{G}_v^{\text{T}} \operatorname{vec}\left(\mathbf{G}_4\right) - \mathbf{G}_h^{\text{T}}\mathbf{z}_3 - \mathbf{G}_v^{\text{T}}\mathbf{z}_4. \tag{30}$$

Equation (30) is solved to produce $\mathbf{G}_2$.

C. Optimizing $\mathbf{G}_3$

The equivalent optimization for $\mathbf{G}_3$ is defined as

$$\mathbf{G}_3 = \operatorname*{argmin}_{0 \leq \mathbf{G}_3 \leq 1} \lambda_{\mathrm{M}} \|\mathbf{G}_3\|_{2,1}$$

$$+ \frac{\beta}{2} \|\mathbf{G}_h \operatorname{vec}(\mathbf{G}_2) - \operatorname{vec}(\mathbf{G}_3) + \mathbf{z}_3\|_{\mathrm{F}}^2. \quad (31)$$

According to [52], the solution of (31) is equivalent to the proximal operator of the L_2 norm. Thus, we use a block soft thresholding $soft_a(b)$ to obtain the solution of (31). $soft_x(y)$ is defined as

$$soft_x(y) = \max\left(1 - \frac{x}{\|y\|}, 0\right) y \quad (32)$$

where $soft_x(0) = 0$.

The solution of (31) is given by

$$\mathbf{G}_3 = soft_{\lambda_{\mathrm{M}}/\beta}(\mathbf{G}_h \operatorname{vec}(\mathbf{G}_2) + \mathbf{z}_3). \quad (33)$$

D. Optimizing $\mathbf{G}_4$

The optimization problem of $\mathbf{G}_4$ can be given by

$$\mathbf{G}_4 = \operatorname*{argmin}_{0 \leq \mathbf{G}_4 \leq 1} \lambda_{\mathrm{M}} \|\mathbf{G}_4\|_{2,1}$$

$$+ \frac{\beta}{2} \|\mathbf{G}_v \operatorname{vec}(\mathbf{G}_2) - \operatorname{vec}(\mathbf{G}_4) + \mathbf{z}_4\|_{\mathrm{F}}^2. \quad (34)$$

Similar to the solution of $\mathbf{G}_3$, the solution of $\mathbf{G}_4$ is defined as

$$\mathbf{G}_4 = soft_{\lambda_{\mathrm{M}}/\beta}(\mathbf{G}_v \operatorname{vec}(\mathbf{G}_2) + \mathbf{z}_4). \quad (35)$$

E. Optimizing $\mathbf{G}_5$

The optimization problem of $\mathbf{G}_5$ is written as

$$\mathbf{G}_5 = \operatorname*{argmin}_{0 \leq \mathbf{G}_5 \leq 1} i_+(\mathbf{G}_5) + \frac{\beta}{2} \|\operatorname{vec}(\mathbf{M}_k^{\mathrm{COSI}}) - \operatorname{vec}(\mathbf{G}_5) + \mathbf{z}_5\|_{\mathrm{F}}^2. \quad (36)$$

The solution of $\mathbf{G}_5$ is referred to [52], and is defined as

$$\mathbf{G}_5 = \max\left(\mathbf{M}_k^{\mathrm{COSI}} + \operatorname{vec}^{-1}(\mathbf{z}_5), 0\right). \quad (37)$$

F. Optimizing $\mathbf{z}$

The alternate update is written as

$$\mathbf{z}^{(i+1)} \leftarrow \mathbf{z}^{(i)} + \mathbf{A}\mathbf{x}^{(i+1)} + \mathbf{B}\mathbf{y}^{(i+1)} - \mathbf{C}. \quad (38)$$

Furthermore, the variable $\mathbf{z}_1$, $\mathbf{z}_2$, $\mathbf{z}_3$, $\mathbf{z}_4$, and $\mathbf{z}_5$ are defined as

$$\mathbf{z}_1 \leftarrow \mathbf{z}_1 + \mathrm{r}(\mathbf{D}_k)\mathbf{x} - \operatorname{vec}(\mathbf{G}_1)$$

$$\mathbf{z}_2 \leftarrow \mathbf{z}_2 + \mathbf{x} - \operatorname{vec}(\mathbf{G}_2)$$

$$\mathbf{z}_3 \leftarrow \mathbf{z}_3 + \mathbf{G}_h \operatorname{vec}(\mathbf{G}_2) - \operatorname{vec}(\mathbf{G}_3)$$

$$\mathbf{z}_4 \leftarrow \mathbf{z}_4 + \mathbf{G}_v \operatorname{vec}(\mathbf{G}_2) - \operatorname{vec}(\mathbf{G}_4)$$

$$\mathbf{z}_5 \leftarrow \mathbf{z}_5 + \mathbf{x} - \operatorname{vec}(\mathbf{G}_5). \quad (39)$$

REFERENCES

[1] Q. Wang, Y. Tang, X. Tong, and P. M. Atkinson, "Virtual image pair-based spatio-temporal fusion," *Remote Sens. Environ.*, vol. 249, 2020, Art. no. 112009.

[2] R. S. Lunetta, J. F. Knight, J. Ediriwickrema, J. G. Lyon, and L. D. Worthy, "Land-cover change detection using multi-temporal MODIS NDVI data," *Remote Sens. Environ.*, vol. 105, no. 2, pp. 142–154, Nov. 2006.

[3] Y. Chen, K. Shi, Y. Ge, and Y. Zhou, "Spatiotemporal remote sensing image fusion using multiscale two-stream convolutional neural networks," *IEEE Trans. Geosci. Remote Sens.*, vol. 60, 2022, Art. no. 4402112.

[4] Q. Wang, X. Ding, X. Tong, and P. M. Atkinson, "Spatio-temporal spectral unmixing of time-series images," *Remote Sens. Environ.*, vol. 259, 2021, Art. no. 11240.

[5] B. Du, M. Zhang, L. Zhang, R. Hu, and D. Tao, "PLTD: Patch-based low-rank tensor decomposition for hyperspectral images," *IEEE Trans. Multimedia*, vol. 19, no. 1, pp. 67–79, Jan. 2017.

[6] J. Verhoeye and R. De Wulf, "Land-cover mapping at sub-pixel resolutions using linear optimization techniques," *Remote Sens. Environ.*, vol. 79, no. 1, pp. 96–104, 2002.

[7] M. Q. Nguyen, P. M. Atkinson, and H. G. Lewis, "Superresolution mapping using hopfield neural network with LIDAR data," *IEEE Geosci. Remote Sens. Lett.*, vol. 2, no. 3, pp. 366–370, Jul. 2005.

[8] X. Zhang, X. Jiang, J. Jiang, Y. Zhang, X. Liu, and Z. Cai, "Spectral–spatial and superpixelwise PCA for unsupervised feature extraction of hyperspectral imagery," *IEEE Trans. Geosci. Remote Sens.*, vol. 60, 2022, Art. no. 5502210.

[9] S. Jia and Y. Qian, "Spectral and spatial complexity-based hyperspectral unmixing," *IEEE Trans. Geosci. Remote Sens.*, vol. 45, no. 12, pp. 3867–3879, Dec. 2006.

[10] L. Wang, D. Liu, and Q. Wang, "Spectral unmixing model based on least squares support vector machine with unmixing residue constraints," *IEEE Geosci. Remote Sens. Lett.*, vol. 10, no. 6, pp. 1592–1596, Nov. 2013.

[11] F. Ling, W. Li, Y. Du, and X. Li, "Land cover change mapping at the subpixel scale with different spatial-resolution remotely sensed imagery," *IEEE Geosci. Remote Sens. Lett.*, vol. 8, no. 1, pp. 182–186, Jan. 2011.

[12] Q. Wang, W. Shi, and P. M. Atkinson, "Spatiotemporal subpixel mapping of time-series images," *IEEE Trans. Geosci. Remote Sens.*, vol. 54, no. 9, pp. 5397–5411, Sep. 2016.

[13] R. Fan, R. Feng, W. Han, and L. Wang, "Urban functional zone mapping with a bibranch neural network via fusing remote sensing and social sensing data," *IEEE J. Sel. Topics Appl. Earth Observ. Remote Sens.*, vol. 14, pp. 11737–11749, 2021.

[14] P. Wang, G. Zhang, and H. Leung, "Improving super-resolution flood inundation mapping for multispectral remote sensing image by supplying more spectral information," *IEEE Geosci. Remote Sens. Lett.*, vol. 6, no. 15, pp. 771–775, May 2019.

[15] F. Ling, Y. Du, Y. Zhang, X. Li, and F. Xiao, "Burned-area mapping at the subpixel scale with MODIS images," *IEEE Geosci. Remote Sens. Lett.*, vol. 12, no. 9, pp. 1963–1967, Sep. 2015.

[16] Y. Zhang, P. M. Atkinson, X. Li, F. Ling, Q. Wang, and Y. Du, "Learning-based spatial–temporal superresolution mapping of forest cover with MODIS images," *IEEE Trans. Geosci. Remote Sens.*, vol. 55, no. 1, pp. 600–614, Jan. 2017.

[17] K. Wu and Q. Du, "Subpixel change detection of multitemporal remote sensed images using variability of endmembers," *IEEE Geosci. Remote Sens. Lett.*, vol. 14, no. 6, pp. 796–800, Jun. 2017.

[18] P. M. Atkinson, "Mapping Sub-pixel boundaries from remotely sensed images," in *Proc. Innovations GIS*, 1997, pp. 166–180.

[19] Q. Wang, W. Shi, and L. Wang, "Allocating classes for soft-then-hard subpixel mapping algorithms in units of class," *IEEE Trans. Geosci. Remote Sens.*, vol. 5, no. 5, pp. 2940–2959, May 2014.

[20] Q. Wang, C. Zhang, X. Tong, and P. M. Atkinson, "General solution to reduce the point spread function effect in subpixel mapping," *Remote Sens. Environ.*, vol. 251, 2020, Art. no. 112054.

[21] X. Xu, X. Tong, A. Plaza, Y. Zhong, and L. Zhang, "Using linear spectral unmixing for sub-pixel mapping of hyperspectral imagery: A quantitative assessment," *IEEE J. Sel. Topics Appl. Earth Observ. Remote Sens.*, vol. 10, no. 4, pp. 1589–1600, Apr. 2017.

[22] X. Xu, X. Tong, A. Plaza, J. Li, Y. Zhong, and L. Zhang, "A new spectral-spatial sub-pixel mapping model for remotely sensed hyperspectral imagery," *IEEE J. Sel. Topics Appl. Earth Observ. Remote Sens.*, vol. 56, no. 11, pp. 6763–6778, Nov. 2018.

[23] L. Li, Y. Chen, X. Yu, R. Liu, and C. Huang, "Sub-pixel flood inundation mapping from multispectral remotely sensed images based on discrete particle swarm optimization," *ISPRS J. Photogrammetry*, vol. 101, pp. 10–21, 2015.

[24] D. Nigussie, R. Zurita-Milla, and J. G. P. W. Clevers, "Possibilities and limitations of artificial neural networks for subpixel mapping of land cover," *Int. J. Remote Sens.*, vol. 32, no. 22, pp. 7203–7226, 2011.

[25] Y. Shao and R. S. Lunetta, "Sub-pixel mapping of tree canopy, impervious surfaces, and cropland in the laurentian great lakes basin using MODIS time-series data," *IEEE J. Sel. Topics Appl. Earth Observ. Remote Sens.,* vol. 4, no. 2, pp. 336–347, Jun. 2011.

[26] L. Lu, Y. Hang, L. Di, and D. Huang, "A new spatial attraction model for improving subpixel land cover classification," *Remote Sens.*, vol. 9, Apr. 2017, Art. no. 360.

[27] P. Wang, L. Wang, H. Leung, and G. Zhang, "Super-resolution mapping based on spatial-spectral correlation for spectral imagery," *IEEE Trans. Geosci. Remote Sens.*, vol. 59, no. 3, pp. 2256–2268, Mar. 2021.

[28] X. Li, Y. Du, F. Ling, Q. Feng, and B. Fu, "Superresolution mapping of remotely sensed image based on hopfield neural network with anisotropic spatial dependence model," *IEEE Geosci. Remote Sens. Lett.,* vol. 11, no. 7, pp. 1265–1269, Jul. 2014.

[29] P. Wang, L. Wang, H. Leung, and G. Zhang, "Subpixel mapping based on hopfield neural network with more prior information," *IEEE Geosci. Remote Sens. Lett.,* vol. 16, no. 8, pp. 1284–1288, Aug. 2019.

[30] Q. Wang, W. Shi, and P. M. Atkinson, "Sub-pixel mapping of remote sensing images based on radial basis function interpolation," *ISPRS J. Photogrammetry*, vol. 92, pp. 1–15, Jun. 2014.

[31] P. Wang, L. Wang, and J. Chanussot, "Soft-then-hard subpixel land cover mapping based on spatial-spectral interpolation," *IEEE Geosci. Remote Sens. Lett.*, vol. 13, no. 12, pp. 1851–1854, Dec. 2016.

[32] H. Jin, G. Mountrakis, and P. Li, "A super-resolution mapping method using local indicator variograms," *Int. J. Remote Sens.*, vol. 33, no. 24, pp. 7747–7773, Dec. 2012.

[33] Q. Wang, P. M. Atkinson, and W. Shi, "Indicator cokriging-based subpixel mapping without prior spatial structure information," *IEEE Trans. Geosci. Remote Sens.*, vol. 53, no. 1, pp. 309–323, Jan. 2015.

[34] Y. Chen, Y. Ge, G. B. M. Heuvelink, R. An, and Y. Chen, "Object-based superresolution land-cover mapping from remotely sensed imagery," *IEEE Trans. Geosci. Remote Sens.*, vol. 56, no. 1, pp. 328–340, Jan. 2018.

[35] P. Wang, H. Yao, C. Li, G. Zhang, and H. Leung, "Multiresolution analysis based on dual-scale regression for pansharpening," *IEEE Trans. Geosci. Remote Sens.*, vol. 60, 2022, Art. no. 5406319.

[36] Y. Ge, Y. Chen, A. Stein, S. Li, and J. Hu, "Enhanced sub-pixel mapping with spatial distribution patterns of geographical objects," *IEEE Trans. Geosci. Remote Sens.*, vol. 54, no. 4, pp. 2356–2370, Jan. 2016.

[37] Q. Wang, W. Shi, P. M. Atkinson, and H. Zhang, "Class allocation for soft-then-hard subpixel mapping algorithms with adaptive visiting order of classes," *IEEE Geosci. Remote Sens. Lett.*, vol. 11, no. 9, pp. 1494–1498, Sep. 2014.

[38] Y. Chen, Y. Ge, G. B. M. Heuvelink, J. Hu, and Y. Jiang, "Hybrid constraints of pure and mixed pixels for soft-then-hard super-resolution mapping with multiple shifted images," *IEEE J. Sel. Topics Appl. Earth Observ. Remote Sens.*, vol. 8, no. 5, pp. 2040–2052, Apr. 2015.

[39] F. Ling and G. M. Foody, "Super-resolution land cover mapping by deep learning," *Remote Sens. Lett.,* vol. 10, no. 6, pp. 598–606, Jun. 2019.

[40] P. Wang, G. Zhang, L. Wang, H. Leung, and H. Bi, "Sub-pixel land cover mapping based on dual processing paths for hyperspectral image," *IEEE J. Sel. Topics Appl. Earth Observ. Remote Sens.,* vol. 12, no. 6, pp. 1835–1848, Jun. 2019.

[41] Y. Chen, G. Wu, Y. Ge, and K. Xu, "Mapping gridded gross domestic product distribution of China using deep learning with multiple geospatial big data," *IEEE J. Sel. Topics Appl. Earth Observ. Remote Sens.*, vol. 15, pp. 1791–1802, Feb. 2022.

[42] P. M. Atkinson, "Sub-pixel target mapping from soft-classified, remotely sensed imagery," *Photogramm. Eng. Remote Sens.,* vol. 71, no. 7, pp. 839–846, Jul. 2005.

[43] F. Ling, W. Li, Y. Du, and X. Li, "Land cover change mapping at the subpixel scale with different spatial-resolution remotely sensed imagery," *IEEE Geosci. Remote Sens. Lett.*, vol. 8, no. 1, pp. 182–186, Jan. 2011.

[44] K. Wu, Y. Wang, R. Q. Niu, and L. F. Wei, "Subpixel land cover change mapping with multitemporal remote-sensed images at different resolution," *J. Appl. Remote Sens.*, vol. 9, no. 1, Dec. 2014, Art. no. 097299.

[45] Q. Wang, P. M. Atkinson, and W. Shi, "Fast subpixel mapping algorithms for subpixel resolution change detection," *IEEE Trans. Geosci. Remote Sens.*, vol. 53, no. 4, pp. 1692–1706, Apr. 2015.

[46] Q. Wang, W. Shi, P. M. Atkinson, and Z. Li, "Land cover change detection at subpixel resolution with a hopfield neural network," *IEEE J. Sel. Topics Appl. Earth Observ. Remote Sens.*, vol. 8, no. 3, pp. 1339–1352, Mar. 2015.

[47] F. Ling, X. Li, Y. Du, and F. Xiao, "Super-resolution land cover mapping with spatial–temporal dependence by integrating a former fine resolution map," *IEEE J. Sel. Topics Appl. Earth Observ. Remote Sens.*, vol. 7, no. 5, pp. 1816–1825, May 2014.

[48] F. Ling, W. Li, Y. Du, and L. X, "Land cover change mapping at the subpixel scale with different spatial-resolution remotely sensed imagery," *IEEE Geosci. Remote Sens. Lett.,* vol. 8, no. 1, pp. 182–186, Jan. 2011.

[49] P. Wang, X. Shen, and G. Zhang, "Spatiotemporal super-resolution mapping by considering the point spread function effect," *IEEE Geosci. Remote Sens. Lett.*, vol. 19, 2022, Art. no. 6001705.

[50] D. He, Y. Zhong, and L. Zhang, "Spectral–spatial–temporal MAP-based sub-pixel mapping for land-cover change detection," *IEEE Trans. Geosci. Remote Sens.*, vol. 58, no. 3, pp. 1696–1717, Mar. 2020.

[51] S. Boyd, N. Parikh, E. Chu, B. Peleato, and J. Eckstein, "Distributed optimization and statistical learning via the alternating direction method of multipliers," *Found. Trends Mach. Learn.*, vol. 3, no. 1, pp. 1–122, 2011.

[52] L. Drumetz, M.-A. Veganzones, S. Henrot, R. Phlypo, J. Chanussot, and C. Jutten, "Blind hyperspectral unmixing using an extended linear mixing model to address spectral variability," *IEEE Trans. Image Process.*, vol. 25, no. 8, pp. 3890–3905, Aug. 2016.

[53] D. C. Heinz and C.-I. Chang, "Fully constrained least squares linear spectral mixture analysis method for material quantification in hyperspectral imagery," *IEEE Trans. Geosci. Remote Sens.,* vol. 39, no. 12, pp. 529–545, Mar. 2001.

Peng Wang (Member, IEEE) received the B.E. degree in microelectronics and Ph.D. degrees in information and communications engineering from the College of Information and Communications Engineering, Harbin Engineering University, Harbin, China, in 2012 and 2018, respectively.

He is currently an Associate Professor with the College of Electronic and Information Engineering, Nanjing University of Aeronautics and Astronautics, Jiangsu, China. He has authored two books and more than 50 articles. His research interests include remote-sensing imagery processing and machine learning.

Mingxuan Huang received the B.E. degree in electronic information engineering from the Nanjing University of Posts and Telecommunications, Nanjing, China, in 2022. She is currently working toward the M.S. degree in electronic information engineering with the College of Electronic and Information Engineering, Nanjing University of Aeronautics and Astronautics, Jiangsu, China.

Her research interest includes remote sensing image processing.

Liguo Wang received the M.S. and Ph.D. degrees in signal and information processing from the Harbin Institute of Technology, Harbin, China, in 2002 and 2005, respectively.

From 2006 to 2008, he was a Postdoctoral Researcher with the College of Information and Communications Engineering, Harbin Engineering University, Harbin. He is currently a Distinguished Professor with Dalian Minzu University, Dalian, China. He has authored three books about hyperspectral image processing and more than 180 papers. His current research interests include remote sensing and machine learning.
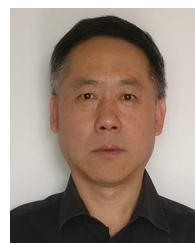
Gong Zhang (Member, IEEE) received the Ph.D. degree in electronic engineering from the Nanjing University of Aeronautics and Astronautics (NUAA), Nanjing, China, in 2002.

From 1990 to 1998, he was a Member of Technical Staff with the Institute of China Shipbuilding Industry Corporation, Nanjing. Since 1998, he has been working with the College of Electronics and Information Engineering, NUAA, where he is currently a Professor. His research interests include radar signal processing and compressive sensing.

Dr. Zhang is a member of the Committee of Electromagnetic Information, Chinese Society of Astronautics, and a Senior Member of the Chinese Institute of Electronics.
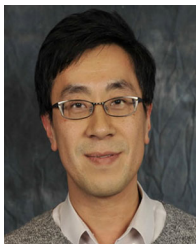
Henry Leung (Fellow, IEEE) received the Ph.D. degree in electrical and computer engineering from the McMaster University, Hamilton, ON, Canada, in 1991.

Before joining University of Calgary, he was with the Department of National Defence of Canada as a Defense Scientist. His research interests include information fusion, machine learning, IoT, nonlinear dynamics, robotics, and signal and image processing.

Prof. Leung is the Associate Editor with the *IEEE Circuits and Systems Magazine*. He is the topic editor on "Robotic Sensors" of the *International Journal of Advanced Robotic Systems*. He is also an Editor of the Springer book series on "Information Fusion and Data Science." In addition, he is a Fellow member of SPIE.

Chunlei Zhao received the B.E. degree in atmospheric science from the Chengdu University of Information Engineering, Chengdu, China, in 2003.

He is currently a Senior Engineer with the Meteorological Institute of Hebei Province. His research interests include meteorological satellite remote sensing and ecological environment monitoring.